









Ab initio and group theoretical study of properties of a carbon trimer defect in hexagonal boron nitride

Omid Golami ^{1,2,*}, Kenneth Sharman ^{1,2}, Roohollah Ghobadi ^{1,2}, Stephen C. Wein ^{1,2}, Hadi Zadeh-Haghighi ^{1,2},
Claudia Gomes da Rocha ², Dennis R. Salahub ^{1,2,3} and Christoph Simon ^{1,2}

¹*Institute for Quantum Science and Technology, University of Calgary, Calgary, Alberta, Canada T2N 1N4*

²*Department of Physics and Astronomy, University of Calgary, Calgary, Alberta, Canada T2N 1N4*

³*Department of Chemistry, CMS Centre for Molecular Simulation, and Quantum Alberta, University of Calgary, Calgary, Alberta, Canada T2N 1N4*



(Received 19 October 2021; revised 12 April 2022; accepted 14 April 2022; published 2 May 2022)

Hexagonal boron nitride (h-BN) is a promising platform for quantum information processing due to its potential to host optically active defects with attractive optical and spin properties. Recent studies suggest that carbon trimers might be the defect responsible for single-photon emission in the visible spectral range in h-BN. In this theoretical study, we combine group theory together with density-functional theory (DFT) calculations to predict the properties of the neutral C_2C_N carbon trimer defect. We find the multi-electron states of this defect along with possible radiative and nonradiative transitions assisted by the spin-orbit and the spin-spin interactions. We also investigate the Hamiltonian for external magnetic-field and ground-state hyperfine interactions. Lastly, we use the results of our investigation in a Lindblad master-equation model to predict an optically detected magnetic resonance signal and the $g^2(\tau)$ correlation function. Our findings can have important outcomes in quantum information applications such as quantum repeaters used in quantum networks and quantum sensing.

DOI: [10.1103/PhysRevB.105.184101](https://doi.org/10.1103/PhysRevB.105.184101)

I. INTRODUCTION

Color centers as solid-state artificial atoms in systems such as diamond, silicon carbide, and van der Waals materials, have potential applications in quantum technology [1,2]. Many of these color centers are single-photon sources and have good spin properties [3]. Single-photon emitters (SPEs) are a vital part of photonic quantum technologies [4,5], also spins with good spin-photon interfaces are promising candidates for storing information [6]. These make color centers important for various quantum applications, including quantum communication, quantum sensing, and distributed quantum computing.

Ultrabright and polarized single-photon emission from color centers in two-dimensional (2D) hexagonal boron nitride (h-BN) has been recently observed at room temperature [7]. h-BN has attracted attention for several reasons. First, it has a relatively large band gap of around 6 eV [8–10] which allows it to host many defects [11–15]. However, the true atomic structure of most of these emitters remains unknown [16,17]. Second, because of its 2D nature, it is promising for heterogeneous assembly and on-chip integration into devices [18,19]. Third, some defects in h-BN might have high sensitivity to the environment because of their location at the surface, which is advantageous for quantum sensing applications [20]. Finally, defects in h-BN are the only known solid-state sources that can display Fourier transform limited lines at room temperature [21]. If the Fourier transform of an emitter's temporal profile matches its spectral lineshape, then

the emitter resonance does not fluctuate during the timescale of emission. This implies that quantum coherence is maintained so that the emitter can be used for many quantum protocols.

It has been shown that visible range SPEs in h-BN originate from carbon-related defects [16]. Jara *et al.* [22] suggest that the neutral C_2C_N and C_2C_B carbon trimer defects might have zero-phonon line (ZPL) energies of 1.62 and 1.65 eV, respectively, and a phonon sideband of around 160 meV, which is typically found in many experiments [16,23]. However, a new study suggests that the C_2C_B defect might have a ZPL energy of 1.36 eV [24]. This energy is too far from the visible range, and so we focus only on the C_2C_N defect where both studies agree on a ZPL energy of around 1.6 eV.

In this study, we explore the electronic structure of the C_2C_N defect in 2D h-BN and find the possible radiative and nonradiative transitions to model the observed lines. To do so, we combine group theory analysis with density-functional theory (DFT) calculations [25,26]. We determine the symmetry-adapted molecular orbitals (MOs) using group theory analysis. Then, we use DFT results to determine the relative energy ordering of these orbitals [27]. Next, we obtain the total orbital and spin multi-electron states by filling the lowest energy MOs, which gives us the ground state. Exciting electrons to the higher energy MOs gives us the excited states [28]. We calculate the total energy of the electronic structures with DFT, and the difference between these energies gives us the transition energies between defect states.

We then consider the spin-orbit, the spin-spin, and external magnetic-field interactions and find matrix elements of the Hamiltonian, where group theory decreases the complexity by

*Corresponding author: Omid.aligholamioskoo@ucalgary.ca

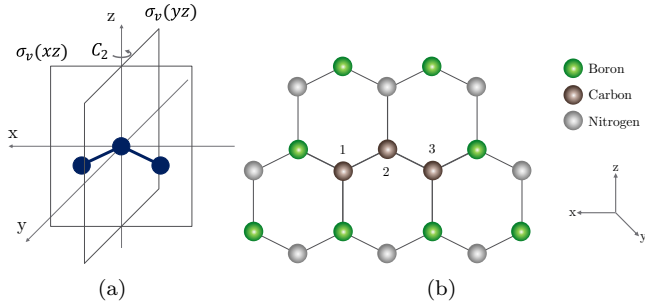


FIG. 1. (a) Symmetry operators of C_{2v} point group, apart from the identity operator (E), shown for a carbon trimer defect. The first one is $C_2(z)$ which is a rotation by π around the z axis. The other two are reflections through xz and yz planes, respectively, $\sigma_v(xz)$ and $\sigma_v(yz)$. Note that the three carbon atoms are in the xz plane. (b) The atomic configuration of the C_2C_N defect in 2D h-BN sheet.

reducing the number of nonzero elements. Furthermore, we look at the interaction between the defect and the electromagnetic field and find nonvanishing matrix elements to derive the optical transitions. Combining this with the spin-orbit and the spin-spin Hamiltonians gives us possible nonradiative transitions assisted by the spin-orbit and the spin-spin interactions [17]. We also examine the hyperfine interaction of the ground state with a possible nearby nuclear spin [29]. Finally, we look at the dynamics of this system and simulate the optically detected magnetic resonance (ODMR) signal predicted by the Lindblad master equation [30].

This paper is organized as follows: In Sec. II we discuss the symmetry of the C_2C_N defect and determine the symmetry-adapted MOs. Then we investigate multi-electron states (Sec. III), the spin-orbit interaction (Sec. IV), the spin-spin interaction (Sec. V), spin-orbit and spin-spin mediated transitions (Sec. VI), selection rules for the transitions (Sec. VII), external magnetic-field effect (Sec. VIII), and hyperfine interaction (Sec. IX). In Sec. X we found radiative

and some nonradiative transition rates, then in Sec. XI we simulate the ODMR spectra and the $g^2(\tau)$ second-order correlation function. Next, we provide a summary in Sec. XIII. Finally, we discuss computational methods in Sec. XII. Matrix elements of all of the interactions and more configurations for the ODMR simulations are given in the Appendix.

II. MOLECULAR ORBITALS

The atomic configuration of the C_2C_N defect is shown in Fig. 1(b), where C_2 denotes the $C_B C_N$ carbon dimer, and C_N denotes a substitution of a nitrogen atom with a carbon atom. To find the symmetry group of the defect, it is important to know if the defect is in- or out-of-plane, as some defects might be distorted out of the plane [31]. A recent study suggests that distortion from the plane for the C_2C_N defect is negligible and that it has a planar structure [24]. Thus, this defect has C_{2v} symmetry, which is supported by defect wave functions as in Fig. 2(a).

The ground-state configuration of carbon is $1s^2 2s^2 2p^2$. The planarity of the defect implies that carbon atoms will have sp^2 hybridization. In sp^2 hybridization, the $2s$ orbital is mixed with only two of the three available $2p$ orbitals. The third $2p$ orbital remains unhybridized and out of the plane and in the \hat{y} direction, which is also confirmed by our DFT calculations shown in Fig. 2(a).

Each carbon atom of the C_2C_N defect shares three of its valence electrons with nearby atoms in the lattice; therefore, they each have one unpaired electron. Thus, the dangling bonds of the defect are π bonds, and they are denoted $\{\pi_1, \pi_2, \pi_3\}$.

Now, we need to find the symmetry-adapted MOs of this defect. The MOs are eigenfunctions of the Coulombic Hamiltonian. We apply the projection operator,

$$\phi_r = P^{(r)} \sigma_i = \frac{l_r}{h} \sum_e \chi_e^{(r)} R_e \pi_i, \quad (1)$$

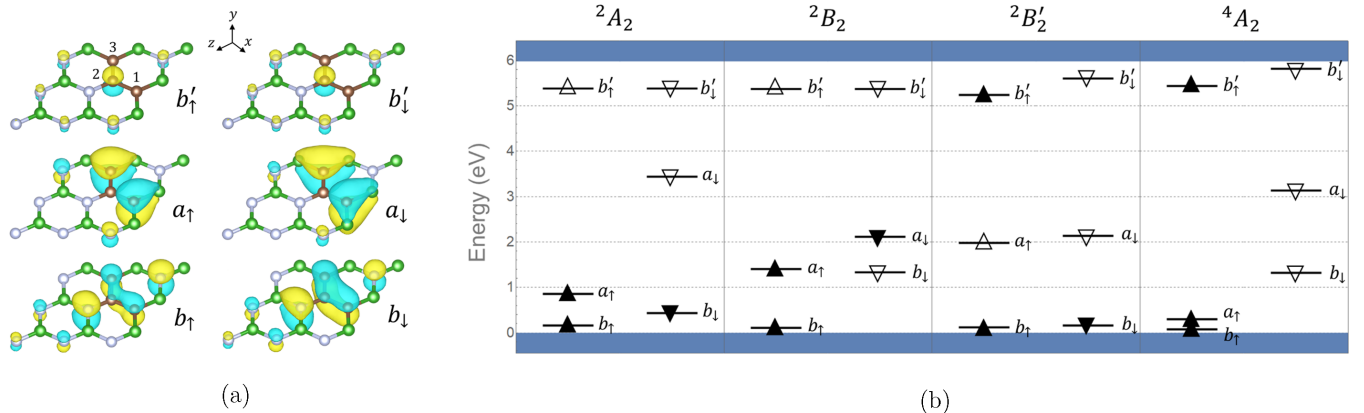


FIG. 2. (a) Ground-state wave functions of the C_2C_N defect. The positive (negative) components of each wave function are visualized by the yellow (blue) lobes. The corresponding symmetries are best represented when the b and a orbitals are plotted here at an isosurface level of $\pm 0.007 \text{ \AA}^{-3}$, and the b' orbital at $\pm 0.0002 \text{ \AA}^{-3}$. The orbital energies increase from the bottom to the top, i.e., $E_b < E_a < E_{b'}$. Only the atoms and contributions to the wave function which are close to the C_2C_N defect are shown for simplicity. The carbon atoms are brown, boron atoms are green, and nitrogen atoms are grey. The diagrams were produced using VESTA [33]. (b) Defect levels of the ground state and single-configuration excited states in the fundamental bandgap of h-BN. The occupied (unoccupied) levels are denoted by solid (empty) triangles.

TABLE I. Character table for C_{2v} point group. E , $C_2(z)$, $\sigma_v(xz)$, $\sigma_v(yz)$ are symmetry operators. A_1 , B_2 , B_1 , and A_2 are irreducible representations of the point group.

C_{2v}	E	$C_2(z)$	$\sigma_v(xz)$	$\sigma_v(yz)$	Linear	Quadratic	Cubic
A_1	1	1	1	1	z	x^2, y^2, z^2	z^3, x^2z, y^2z
B_2	1	-1	-1	1	y, R_x	yz	yz^2, y^3, x^2y
B_1	1	-1	1	-1	x, R_y	xz	xz^2, x^3, xy^2
A_2	1	1	-1	-1	R_z	xy	xyz

with a specific irreducible representation (IR) on our dangling bonds to find symmetrized MOs [32]. Here, $P^{(r)}$ is the projection to the representation r , l_r is the dimension of the representation r , h is the number of symmetry group members, $\chi_e^{(r)}$ is the character of the operator e in the representation r , R_e is the symmetry operator, and π_i is the dangling bond i . According to the character table of the C_{2v} point group (Table I), b and b' MOs transform according to IR B_2 . They are defined as

$$b = \alpha\pi_2 + \frac{\beta}{\sqrt{2}}(\pi_1 + \pi_3), \quad (2)$$

$$b' = \beta\pi_2 + \frac{\alpha}{\sqrt{2}}(\pi_1 + \pi_3), \quad (3)$$

where α and β are overlap integrals and $|\alpha|^2 + |\beta|^2 = 1$. There is another MO that transforms as IR A_2 , defined as

$$a = \frac{1}{\sqrt{2}}\{\pi_1 - \pi_3\}. \quad (4)$$

III. MULTI-ELECTRON STATES

We use DFT to find the energy of each of the MOs discussed above and their energy ordering. The defect wave functions in Fig. 2(a) obtained from the DFT calculations show that the MO with the lowest energy transforms as IR B_2 , so it represents the b MO. This is because, according to the symmetry operators in Fig. 1(a), this MO is antisymmetric under $C_2(z)$ and $\sigma_v(xz)$, and symmetric under E and $\sigma_v(yz)$. The next MO with higher-energy transforms as IR A_2 , because it is antisymmetric under $\sigma_v(xz)$ and $\sigma_v(yz)$, and symmetric under E and $C_2(z)$. Therefore, it represents the a MO. Finally, the one with the highest energy transforms as IR B_2 similar to the first one, and thus it represents the b' MO. Based on a previous study, the MOs in the ground state and the first-excited state lie inside the band gap [22]. Our *ab initio* calculations show that the MOs in the next two excited states are also in the band gap.

Multi-electron states are composed by filling the MOs with three unpaired electrons of the defect, starting from the lowest energy b MO. The b MO will be fully occupied with two electrons in the ground state, and the a MO will be half occupied. This configuration will form a spin doublet because the half occupied a MO can be either spin up or down. So its spin multiplicity will be equal to two. This lowest multi-electron state has the configuration $[b]^2[a]^1[b']^0$ which transforms as IR A_2 . Other excited multi-electron states are produced by exciting each of these electrons to higher MOs. The $[b]^1[a]^2[b']^0$

TABLE II. Configuration of total wave functions. Some of these states are entangled states which need careful consideration when calculating their energy using DFT. Spin-down electrons in an orbital are shown with a line over them. In the label column, calligraphic letters \mathcal{A} and \mathcal{B} represent IRs A_2 and B_2 , respectively. Also, d and q in the superscript stand for doublet and quartet states, respectively. Prime and double prime in IRs of each state is used just to distinguish them with other states with the same IR.

Configuration	$2S+1\Gamma$	Clebsch-Gordan states	Label
$[b]^2[a]^1[b']^0$	2A_2	$ \bar{b}\bar{b}a\rangle, \bar{b}\bar{b}\bar{a}\rangle$	$\mathcal{A}_{\pm 1/2}^{0,d}$
$[b]^1[a]^2[b']^0$	2B_2	$ ba\bar{a}\rangle, \bar{b}\bar{a}\bar{a}\rangle$	$\mathcal{B}_{\pm 1/2}^{1,d}$
$[b]^2[a]^0[b']^1$	$^2B'_2$	$ b\bar{b}\bar{b}'\rangle, \bar{b}\bar{b}\bar{b}'\rangle$	$\mathcal{B}_{\pm 1/2}^{2,d}$
$[b]^1[a]^1[b']^1$	4A_2	$ bab'\rangle, \bar{b}\bar{a}\bar{b}'\rangle$	$\mathcal{A}_{\pm 3/2}^{3,q}$
		$\frac{1}{\sqrt{3}}(\bar{b}\bar{a}b'\rangle + \bar{b}\bar{a}\bar{b}'\rangle + \bar{b}\bar{a}\bar{b}'\rangle)$	$\mathcal{A}_{+1/2}^{3,q}$
		$\frac{1}{\sqrt{3}}(\bar{b}\bar{a}\bar{b}'\rangle + \bar{b}\bar{a}\bar{b}'\rangle + \bar{b}\bar{a}\bar{b}'\rangle)$	$\mathcal{A}_{-1/2}^{3,q}$
	$^2A'_2$	$\frac{1}{\sqrt{6}}(\bar{b}\bar{a}b'\rangle + \bar{b}\bar{a}\bar{b}'\rangle - 2 \bar{b}\bar{a}\bar{b}'\rangle)$	$\mathcal{A}_{+1/2}^{3,d'}$
		$\frac{1}{\sqrt{6}}(\bar{b}\bar{a}\bar{b}'\rangle + \bar{b}\bar{a}\bar{b}'\rangle - 2 \bar{b}\bar{a}\bar{b}'\rangle)$	$\mathcal{A}_{-1/2}^{3,d'}$
	$^2A''_2$	$\frac{1}{\sqrt{2}}(\bar{b}\bar{a}b'\rangle - \bar{b}\bar{a}\bar{b}'\rangle)$	$\mathcal{A}_{+1/2}^{3,d''}$
		$\frac{1}{\sqrt{2}}(\bar{b}\bar{a}\bar{b}'\rangle - \bar{b}\bar{a}\bar{b}'\rangle)$	$\mathcal{A}_{-1/2}^{3,d''}$

and $[b]^2[a]^0[b']^1$ configurations are also spin doublets, similar to the ground state, and transform according to IR B_2 . But the other excited state $[b]^1[a]^1[b']^1$ needs careful consideration. Since it is the addition of three spin-1/2 orbitals, it will have three irreducible spin representations, including one quartet state and two doublet states with multiplicities four, two, and two, respectively. These states all transform as IR A_2 . The corresponding electronic configurations of these states are given in Table II and the energy levels of the first four single-configuration states are given in Fig. 2(b).

IV. SPIN-ORBIT INTERACTION

The spin-orbit interaction is the sum of the Larmor and Thomas interaction energy which is given by

$$H_{\text{SO}} = \sum_k \frac{\hbar}{2m_e c^2} (\nabla_k V \times \mathbf{p}_k) \cdot \left(\frac{\mathbf{s}_k}{\hbar} \right) = \sum_k \mathbf{l}_k \cdot \left(\frac{\mathbf{s}_k}{\hbar} \right), \quad (5)$$

where V is the electric potential energy of the nucleus, \hbar is the reduced Planck constant, m_e is the electron rest mass, c is the speed of light in vacuum, \mathbf{s}_k is the spin of electron k , \mathbf{p}_k is the momentum of electron k , and k sums over all electrons [28]. By utilizing group theory, we omit the vanishing components of the matrix elements of \mathbf{l}_k . The elements $\langle \phi_i | \mathbf{l}_k | \phi_j \rangle$ are nonvanishing only if $\Gamma(\phi_i) \otimes \Gamma(\mathbf{l}_k) \otimes \Gamma(\phi_j) \supset \Gamma^A$, where Γ is the irreducible representation. Since \mathbf{l} is proportional to $\mathbf{r} \times \mathbf{p}$, it transforms as (B_2, B_1, A_2) . Based on Table III, only l_y , which transforms as IR B_1 , will have nonzero values. Therefore,

$$H_{\text{SO}} = \sum_k l_k^{(y)} \left(\frac{s_k^{(y)}}{\hbar} \right). \quad (6)$$

TABLE III. Matrix elements of operators with specific symmetries in the $\{B_2, A_2\}$ manifold where \times indicates a nonzero value.

O^{A_1}	B_2	A_2
B_2	\times	0
A_2	0	\times
O^{B_2}	B_2	A_2
B_2	0	0
A_2	0	0
O^{B_1}	B_2	A_2
B_2	0	\times
A_2	\times	0
O^{A_2}	B_2	A_2
B_2	0	0
A_2	0	0

Because of the symmetry of the system and according to Table III, we know that only elements in the form of $\langle B_2 | H_{so} | A_2 \rangle$ and their complex conjugate will be nonzero. Also, since we know $s_y = \frac{1}{2i}(s_+ - s_-)$, only the states whose spin are different by one will yield nonzero values. After considering these symmetry constraints, we obtain the matrix elements provided in the Appendix (Sec. A 1).

V. SPIN-SPIN INTERACTION

The spin-spin interaction is described by

$$\begin{aligned}
 H_{ss} &= \frac{\mu_0 \gamma_e^2 \hbar^2}{4\pi} \sum_{i>j} \frac{1}{r_{ij}^3} [s_i \cdot s_j - 3(s_i \cdot \hat{r}_{ij})(s_j \cdot \hat{r}_{ij})] \\
 &= \frac{\mu_0 \gamma_e^2 \hbar^2}{4\pi} \sum_{i>j} [s_i \cdot \hat{D}_{ij} \cdot s_j] \\
 &= \frac{\mu_0 \gamma_e^2 \hbar^2}{4\pi} \sum_{i>j} [\hat{s}_{ij}^{(2)} \otimes \hat{D}_{ij}^{(2)}]^{(0)}, \quad (7)
 \end{aligned}$$

where $r_{ij} = r_i - r_j$ is the distance between electrons i and j , \hat{r}_{ij} is the unit vector from electron i to electron j , s_i is the spin of nucleus i , μ_0 is the vacuum permeability, and γ_e is the electron gyromagnetic ratio [34]. $\hat{s}_{ij}^{(2)} = \hat{s}_i^{(1)} \otimes \hat{s}_j^{(1)}$ is a rank two spin tensor and \hat{D}_{ij} is a traceless second-rank tensor operator defined as,

$$\hat{D}_{ij} = \frac{1}{r_{ij}^5} \begin{pmatrix} r_{ij}^2 - 3x_{ij}^2 & -3x_{ij}y_{ij} & -3x_{ij}z_{ij} \\ -3x_{ij}y_{ij} & r_{ij}^2 - 3y_{ij}^2 & -3y_{ij}z_{ij} \\ -3x_{ij}z_{ij} & -3y_{ij}z_{ij} & r_{ij}^2 - 3z_{ij}^2 \end{pmatrix}. \quad (8)$$

Writing the interaction in this form simplifies the calculations of matrix elements.

For spherically symmetric states, traceless \hat{D}_{ij} means all three diagonal elements vanish. However, due to the lack of spherical symmetry of this defect, we should consider these elements in this magnetic dipole-dipole interaction. More details and matrix elements of the spin-spin Hamiltonian are provided in the Appendix Sec. A 2.

VI. SPIN-ORBIT AND SPIN-SPIN INDUCED TRANSITIONS

For the spin-orbit interaction, as we discussed before, only the matrix elements in the form of $\langle B_2 | H_{so} | A_2 \rangle$ and their complex conjugate will be nonzero. This indicates that there are no matrix elements in degenerate manifolds of $\{\mathcal{A}^{0,d}, \mathcal{B}^{1,d}, \mathcal{B}^{2,d}, \mathcal{A}^{3,q}\}$. Therefore, there is no mixing due to the spin-orbit coupling. However, we have possible spin-orbit-induced transitions between the states in these manifolds, which are $\mathcal{B}^{1,d} \leftrightarrow \mathcal{A}^{0,d}$, $\mathcal{B}^{2,d} \leftrightarrow \mathcal{A}^{0,d}$, $\mathcal{B}^{1,d} \leftrightarrow \mathcal{A}^{3,q}$, and $\mathcal{B}^{2,d} \leftrightarrow \mathcal{A}^{3,q}$. As discussed in Ref. [35,36], these types of transitions can happen in two steps. First, spin-orbit assisted transition occurs for example from $\mathcal{B}^{2,d}$ to a vibrational excited state of $\mathcal{A}^{3,q}$. This is followed by a relaxation to the vibrational ground-state, for example, via the emission of one or more phonons. Such a process will be possible if there is an overlap between the initial vibrational level of $\mathcal{B}^{2,d}$ and the excited vibrational level of $\mathcal{A}^{3,q}$.

Similarly and based on the findings of the previous section, the spin-spin interaction has no matrix element in the degenerate manifold of $\{\mathcal{A}^{0,d}, \mathcal{B}^{1,d}, \mathcal{B}^{2,d}\}$. However, there are nonzero matrix elements of the spin-spin interaction in the quartet-state manifold. \mathcal{D}_0 is the diagonal, and \mathcal{E}_3 is the off-diagonal term. Hence, spin-spin interaction breaks the degenerate quartet states into two states and separates them by $2\mathcal{D}_0$. Also, the nondiagonal terms in the same manifold mix these two states. There are also possible spin-spin induced transitions between the states in these manifolds, which are $\mathcal{A}^{0,d} \leftrightarrow \mathcal{A}^{3,q}$, $\mathcal{B}^{1,d} \leftrightarrow \mathcal{A}^{3,q}$, $\mathcal{B}^{2,d} \leftrightarrow \mathcal{A}^{3,q}$.

VII. SELECTION RULES

Here we look at the dominant transition allowed by the interaction of the electron with the electromagnetic field, which is the electric-dipole transition. The electric-dipole interaction is defined as

$$H_{\text{dipole}} = \mathbf{E} \cdot \mathbf{d} = \sum_k e \mathbf{E} \cdot \mathbf{r}_k, \quad (9)$$

where \mathbf{E} is the electric field, \mathbf{d} is the electric-dipole moment, \mathbf{r}_k is the position of k electron with respect to the nucleus, and e is the elementary electric charge. The position \mathbf{r} in the C_{2v} group transforms like (B_1, B_2, A_1) . Thus, according to Table III, the allowed transitions are induced by either eE_x or eE_z and the dipole moment lies completely in the plane. The dipole allowed transitions and the matrix elements are given in the Appendix (Sec. A 3). These results are summarized in Fig. 3(a), which shows radiative and nonradiative transitions along with the energy levels of the states.

VIII. EXTERNAL MAGNETIC FIELD

In the presence of an external magnetic field, there will be another term for the Zeeman interaction of the magnetic field with spin and orbital angular momentum [27]. This interaction is given by

$$H_B = \frac{e}{2m_e} \sum_k (\mathbf{l}_k + g_e s_k) \cdot \mathbf{B}, \quad (10)$$

where g_e is the electron-spin g factor, s is the electron spin, \mathbf{l} is electron orbital angular momentum, \mathbf{B} is the

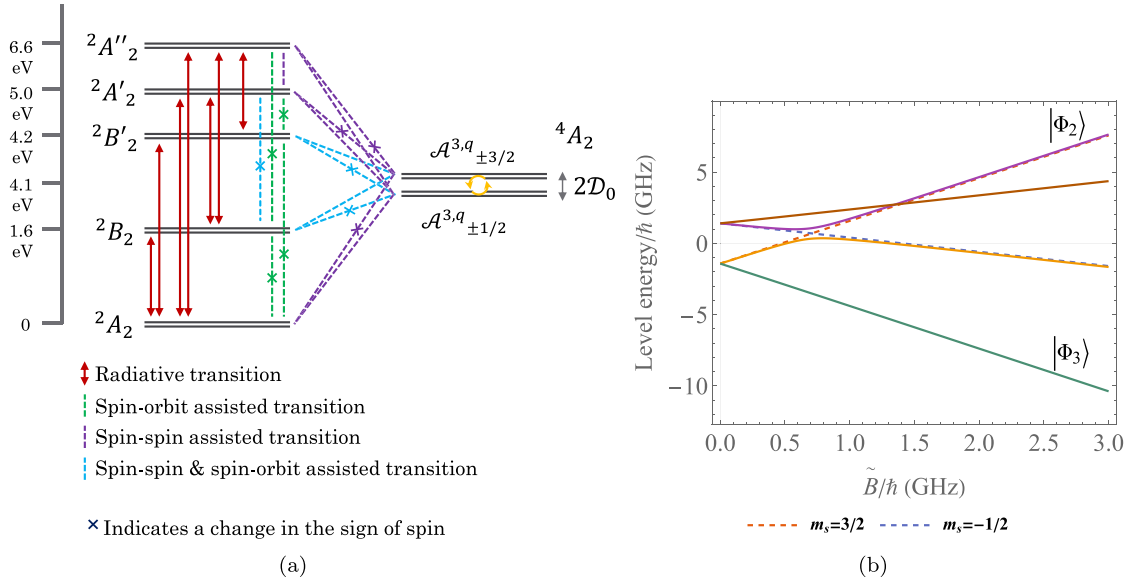


FIG. 3. (a) The electronic structure of the C_2C_N defect and possible radiative and nonradiative transitions. Red lines shows the possible electric-dipole transitions, while dashed lines indicate possible phonon-assisted transitions. Yellow arrows show mixing between $A_{\pm 3/2}^{(3,q)}$ and $A_{\pm 1/2}^{(3,q)}$ due to the spin-spin coupling. The spin-spin coupling splits 4A_2 states by $2\mathcal{D}_0$ if we assume that \mathcal{E}_3 is much smaller than \mathcal{D}_0 . The relative energy spacings of these states were obtained by our DFT calculations, which considers the Coulomb interaction and the HSE06 exchange-correlation functional. In this figure, we have assumed the quartet state is further detuned from the doublets than the spin-orbit coefficient. Usually the spin-orbit coefficient is on the order of GHz [27] and here the closest doublet to the quartet is separated by 0.1 eV, corresponding to 24 THz. (b) The quartet-state anticrossing, which shows an anticrossing between the $|\Phi_1\rangle$ and $|\Phi_2\rangle$ states near $\tilde{B}_y/\hbar = 0.7$ GHz. Here, we have assumed that $\tilde{\mathcal{D}}_0$ and $\tilde{\mathcal{E}}_3$ are equal to 1 GHz. The dashed lines show the behavior of states with $m_s = 3/2$ and $m_s = -1/2$ in the presence of a magnetic field.

external magnetic field, and k sums over all electrons. But since l_z transforms as IR A_2 and l_x transforms as IR B_2 , according to Table III, they do not contribute to the Hamiltonian. Therefore, the Zeeman interaction will be simplified to $H_B = \frac{e}{2m_e} \sum_k [B_x g_e s_{x,k} + B_y (l_{y,k} + g_e s_{y,k}) + B_z g_e s_{z,k}]$. The matrix elements of the Hamiltonian above are given in Appendix B.

A. Quartet-state anticrossing

As we discussed previously, the spin-spin interaction splits and mixes the quartet-state eigenvalues and the spin-orbit interaction does not affect them. Adding a magnetic field perpendicular to the h-BN sheet (\hat{y}) modifies the energy eigenvalues of the quartet state. We add the matrix elements of the interactions for the quartet state from preceding sections and find its eigensystem. The energy eigenvalues are given by

$$\begin{aligned} E_1 &= \tilde{B}_y - \kappa_1, & E_2 &= \tilde{B}_y + \kappa_1, \\ E_3 &= -\tilde{B}_y - \kappa_1, & E_4 &= -\tilde{B}_y + \kappa_1, \end{aligned} \quad (11)$$

and eigenvalues are given by

$$\begin{aligned} |\Phi_1\rangle &= \mu_1 |\mathcal{A}_{-1/2}^{3,q}\rangle + i\mu_1 |\mathcal{A}_{+1/2}^{3,q}\rangle + i |\mathcal{A}_{-3/2}^{3,q}\rangle + |\mathcal{A}_{+3/2}^{3,q}\rangle, \\ |\Phi_2\rangle &= -\mu_2 |\mathcal{A}_{-1/2}^{3,q}\rangle - i\mu_2 |\mathcal{A}_{+1/2}^{3,q}\rangle + i |\mathcal{A}_{-3/2}^{3,q}\rangle + |\mathcal{A}_{+3/2}^{3,q}\rangle, \\ |\Phi_3\rangle &= -\nu_1 |\mathcal{A}_{-1/2}^{3,q}\rangle + i\nu_1 |\mathcal{A}_{+1/2}^{3,q}\rangle - i |\mathcal{A}_{-3/2}^{3,q}\rangle + |\mathcal{A}_{+3/2}^{3,q}\rangle, \\ |\Phi_4\rangle &= -\nu_2 |\mathcal{A}_{-1/2}^{3,q}\rangle + i\nu_2 |\mathcal{A}_{+1/2}^{3,q}\rangle - i |\mathcal{A}_{-3/2}^{3,q}\rangle + |\mathcal{A}_{+3/2}^{3,q}\rangle, \end{aligned} \quad (12)$$

where the coefficients are defined as

$$\begin{aligned} \kappa_1 &= \sqrt{4\tilde{B}_y^2 + \tilde{\mathcal{D}}_0^2 + \tilde{\mathcal{E}}_3^2 - 2\tilde{B}_y(\tilde{\mathcal{D}}_0 + \sqrt{3}\tilde{\mathcal{E}}_3)}, \\ \kappa_2 &= \sqrt{4\tilde{B}_y^2 + \tilde{\mathcal{D}}_0^2 + \tilde{\mathcal{E}}_3^2 + 2\tilde{B}_y(\tilde{\mathcal{D}}_0 + \sqrt{3}\tilde{\mathcal{E}}_3)}, \\ \mu_1 &= \frac{(\sqrt{3}\tilde{B}_y + \tilde{\mathcal{E}}_3)(\kappa_1 - \tilde{B}_y + \tilde{\mathcal{D}}_0)}{3\tilde{B}_y^2 - \tilde{\mathcal{E}}_3^2}, \\ \mu_2 &= \frac{(\sqrt{3}\tilde{B}_y + \tilde{\mathcal{E}}_3)(\kappa_1 + \tilde{B}_y - \tilde{\mathcal{D}}_0)}{3\tilde{B}_y^2 - \tilde{\mathcal{E}}_3^2}, \\ \nu_1 &= \frac{(\sqrt{3}\tilde{B}_y - \tilde{\mathcal{E}}_3)(\kappa_2 + \tilde{B}_y + \tilde{\mathcal{D}}_0)}{3\tilde{B}_y^2 - \tilde{\mathcal{E}}_3^2}, \\ \nu_2 &= \frac{(\tilde{\mathcal{E}}_3 - \sqrt{3}\tilde{B}_y)(-\kappa_2 + \tilde{B}_y + \tilde{\mathcal{D}}_0)}{\tilde{\mathcal{E}}_3^2 - 3\tilde{B}_y^2}. \end{aligned} \quad (13)$$

The variables with tilde are defined as below to simplify the equations.

$$\tilde{B}_y = \frac{\gamma_e \hbar}{2} B_y, \quad \tilde{\mathcal{D}}_0 = \frac{\mu_0 \gamma_e^2 \hbar^2}{16\pi} \mathcal{D}_0, \quad \tilde{\mathcal{E}}_3 = \frac{\mu_0 \gamma_e^2 \hbar^2}{16\pi} \mathcal{E}_3. \quad (14)$$

Based on these results and as shown in Fig. 3(b), an anticrossing happens between $|\Phi_1\rangle$ and $|\Phi_2\rangle$ when the magnetic field compensates the spin-spin splitting at \tilde{B}_y near $(\tilde{\mathcal{D}}_0^2 + \tilde{\mathcal{E}}_3^2)^{1/2}/2$. The $|\Phi_3\rangle$ state, remains unmixed as it is diverging from other states. The $|\Phi_4\rangle$ state is not mixed too, despite the fact that the $|\Phi_2\rangle$ state passes it at \tilde{B}_y near $(\tilde{\mathcal{D}}_0^2 + \tilde{\mathcal{E}}_3^2)^{1/2}$.

IX. GROUND-STATE HYPERFINE INTERACTION

Nuclear spins in solids are a promising candidate for storing information and using them as quantum memories due to their long coherence time [37]. Nuclear-spin quantum memories have been demonstrated experimentally for the orbital ground state of the negatively charged nitrogen-vacancy center in diamond [38,39]. In this section, we investigate the effect of the presence of a carbon-13 nuclear spin in the defect, which is given by $\hat{H} = \hat{H}_{13C} + \hat{V}_{\text{mhf}} + \hat{V}_{\text{chf}}$. The first term is the Zeeman interaction of the nuclear spin with an external magnetic field, which is given by $\hat{H}_{13C} = -\gamma_{13C} \mathbf{B} \cdot \hat{\mathbf{I}}$, where $\hat{\mathbf{I}}$ is the nuclear spin and γ_{13C} is the nuclear-spin gyromagnetic ratio of ^{13}C . The second (third) term is the electric (magnetic) component of the hyperfine interaction of the ground electronic state of the defect with the ^{13}C nuclear spin [29,40]. We only have to look at the magnetic component since ^{13}C has a nuclear spin of $I = 1/2$, and the electric component is due to the quadrupole moment of nuclei with spin $I \geq 1$ [41]. Also, we ignored the nuclear spin-spin interactions in this paper.

The magnetic hyperfine Hamiltonian accounts for the interaction between the nuclear spin and the electronic orbital magnetic moment in addition to the dipole-dipole interaction between the nuclear spin and the electron spin. The component of the hyperfine interaction that is related to the orbital angular momentum is given by $2g_I \mu_N \mu_B \frac{\mu_0 \hbar}{4\pi} \sum_i \frac{1}{r_{iC}^3} \mathbf{I} \cdot \mathbf{L}$, where μ_N is the nuclear magneton, μ_B is the Bohr magneton, g_I is the nuclear g factor, and r_{iC} is the distance between ^{13}C and electron i . This component is zero based on Table III, since our ground states transform as IR B_2 and do not have orbital angular momentum. Hence, we only need to consider the dipole-dipole interaction between the electron spin and the nuclear spin. The magnetic part of the hyperfine Hamiltonian, with these considerations, is given by

$$\begin{aligned} \hat{V}_{\text{mhf}} &= C_{\text{mhf}} \sum_i \left\{ \left(\frac{8\pi}{3} \delta(\hat{r}_{iC}) - \frac{1}{r_{iC}^3} \right) \hat{s}_i \cdot \hat{\mathbf{I}} \right. \\ &\quad \left. + \frac{3(\hat{s}_i \cdot \hat{r}_{iC})(\hat{\mathbf{I}} \cdot \hat{r}_{iC})}{r_{iC}^5} \right\} \\ &= -C_{\text{mhf}} \sum_i \hat{s}_i \cdot \hat{A}_i^{(2)} \cdot \hat{\mathbf{I}} \\ &= -C_{\text{mhf}} \sum_i [\hat{J}_i^{(2)} \otimes \hat{A}_i^{(2)}]^{(0)}, \end{aligned} \quad (15)$$

where $C_{\text{mhf}} = g_I \mu_N g_e \mu_B \frac{\mu_0 \hbar^2}{4\pi}$, and $\hat{A}_i^{(2)}$ is a second rank tensor. The Fermi contact term contributes to the energy of orbitals with nonzero value of the wave function at the position of the nucleus. However, based on our DFT calculations [Fig. 2(a)], the wave functions are zero at the position of the carbon nuclei and we can ignore the Dirac delta term. Consequently, the second-order tensor $\hat{A}_i^{(2)}$ is given by

$$\hat{A}_i^{(2)} = \frac{1}{r_{iC}^5} \begin{pmatrix} r_{iC}^2 - 3x_{iC}^2 & -3x_{iC}y_{iC} & -3x_{iC}z_{iC} \\ -3x_{iC}y_{iC} & r_{iC}^2 - 3y_{iC}^2 & -3y_{iC}z_{iC} \\ -3x_{iC}z_{iC} & -3y_{iC}z_{iC} & r_{iC}^2 - 3z_{iC}^2 \end{pmatrix}. \quad (16)$$

For simplifying further calculations, we define $\hat{J}_i^{(2)} = \hat{s}_i \otimes \hat{\mathbf{I}}$ and write the interaction in the compound tensor form.

TABLE IV. Lifetimes τ_{rad} and rates Γ_{rad} of the radiative transitions used in our ODMR simulation.

Transition	μ	μ [eÅ]	E_{ZPL} [eV]	τ_{rad} [ns]	Γ_{rad}
${}^2B_2 \rightarrow {}^2A_2$	$\langle a_i er b_\downarrow \rangle$	0.68	1.6	64.5	15.5
${}^2B'_2 \rightarrow {}^2A_2$	$\langle b'_i er a_\uparrow \rangle$	0.11	4.2	144.4	6.9

According to Table III, for the ground states $|\mathcal{A}_{\pm 1/2}^{0,d}\rangle$, only the operators of the form O^{A_1} contributes to the hyperfine interaction. Thus, only the diagonal terms of $\hat{A}_i^{(2)}$ in Eq. (16) transform as IR A_1 contribute to the hyperfine interaction of the ground state, and the off-diagonal terms do not contribute. We write the basis of the ground state of the defect coupled to a ^{13}C nuclear spin as

$$\begin{aligned} |\Psi_1^g; 1, +1\rangle &= |\mathcal{A}_{+1/2}^{0,d}\rangle |+\rangle_I, \\ |\Psi_2^g; 1, 0\rangle &= \frac{1}{\sqrt{2}} (|\mathcal{A}_{+1/2}^{0,d}\rangle |-\rangle_I + |\mathcal{A}_{-1/2}^{0,d}\rangle |+\rangle_I), \\ |\Psi_3^g; 1, -1\rangle &= |\mathcal{A}_{-1/2}^{0,d}\rangle |-\rangle_I, \\ |\Psi_4^g; 0, 0\rangle &= \frac{1}{\sqrt{2}} (|\mathcal{A}_{+1/2}^{0,d}\rangle |-\rangle_I - |\mathcal{A}_{-1/2}^{0,d}\rangle |+\rangle_I). \end{aligned} \quad (17)$$

Based on the symmetry of the system, there can only be nonzero hyperfine matrix elements for states that have $\Delta S \in \{0, \pm 2\}$. The results of the calculations for matrix elements are shown in the Appendix [Sec. (C2)].

X. TRANSITION RATES

Here we show our results for the radiative and the electron-phonon induced nonradiative transition rates between the $\{{}^2A_2, {}^2B_2, {}^2B'_2\}$ doublet states. The results of the calculations are presented in the following sections.

A. Radiative rates

The radiative transitions occur at a rate given by

$$\Gamma_{\text{rad}} = \frac{1}{\tau_{\text{rad}}} = \frac{nE_{\text{ZPL}}^3 \mu^2}{3\pi \epsilon_0 c^3 \hbar^4}, \quad (18)$$

where n is the refractive index of h-BN, E_{ZPL} is the zero-phonon transition energy, μ is the transition dipole moment, and ϵ_0 is the vacuum permittivity [42,43]. The refractive index of h-BN is taken to be $n = 2.1$ [44]. Equation (18) was evaluated for the ${}^2B_2 \rightarrow {}^2A_2$ and ${}^2B'_2 \rightarrow {}^2A_2$ transitions, which amounts to calculating the corresponding transition dipole moments. The wfck2r.x module in QUANTUM ESPRESSO was used to produce the spin-polarized, real-space wave functions, from which the transition dipole moments were directly computed. Table IV summarizes the results.

B. Nonradiative rates

The nonradiative rates due to electron-phonon coupling can be calculated within the static coupling and one-dimensional effective phonon approximations [45,46]. The nonradiative transition rate between an initial electron state i and a final

TABLE V. Nonradiative recombination properties within the static coupling and one-dimensional effective phonon approximations, evaluated at 300 K. The relaxed atomic coordinates of the ground state are set to $Q_0 = 0$, from which the excited-state equilibrium coordinates are offset by ΔQ . For completeness, we have included the ground-state Huang-Rhys factor which quantifies strength of the electron-phonon coupling, as computed in the one-dimensional approximation, $S_f = (\Delta Q)^2 \Omega_f / 2\hbar$.

Transition	E_{ZPL} [eV]	ΔQ [amu ^{1/2} Å]	$\hbar\omega_i$ [meV]	$\hbar\omega_f$ [meV]	S_f	X_{if} [amu Å ² eV ⁻¹]	W_{if} [eV amu ^{-1/2} Å ⁻¹]	τ_{nr} [ms]	Γ_{nr} [kHz]
${}^2B_2 \rightarrow {}^2A_2$	1.6	0.36	95.7	95.4	1.49	3.66×10^{-11}	5.40×10^{-2}	0.5	2
${}^2B'_2 \rightarrow {}^2A_2$	4.2	0.21	91.8	94.9	0.52	2.31×10^{-20}	3.55×10^{-1}	$>10^3$	$<10^{-3}$

electron state f is given by

$$\Gamma_{nr} = \frac{1}{\tau_{nr}} = \frac{2\pi}{\hbar} g |W_{if}|^2 X_{if}, \quad (19)$$

where g is the degeneracy of the final state. Equation (19) includes contributions from a phonon term X_{if} and an electronic term W_{if} . The phonon term is given by

$$X_{if} = \sum_{n,m} p_{in} |\langle \chi_{fm} | Q - Q_0 | \chi_{in} \rangle|^2 \delta(E_{ZPL} + m\hbar\Omega_f - n\hbar\Omega_i), \quad (20)$$

where Q is the generalized coordinate defined in Ref. [45], and Q_0 is taken to be the relaxed atomic coordinates of the final electronic state (\mathbf{R}_0). Here, p_{in} is the thermal occupation of the phonon state n in the electronic state i , $|\chi_{jk}\rangle$ is the phonon wave function of the phonon state k in the electronic state j , and $\hbar\Omega_{\{i,f\}}$ are the effective phonon energies of the initial and final states. The phonon overlap can be calculated directly using the quantum harmonic-oscillator wave functions. The electronic term is given by

$$W_{if} = \langle \psi_i(\mathbf{r}, \mathbf{R}) | \frac{\partial H}{\partial Q} | \psi_f(\mathbf{r}, \mathbf{R}) \rangle_{\mathbf{R}=\mathbf{R}_0}, \quad (21)$$

which can be calculated numerically by finite differences using the DFT single-particle wave functions at the Γ point [45,47]. The nonradiative rates for the ${}^2B_2 \rightarrow {}^2A_2$ and ${}^2B'_2 \rightarrow {}^2A_2$ transitions were computed by modifying the open-source NONRAD code [47]. The results are summarized in Table V, which shows that the nonradiative rates are negligible compared with the radiative rates. The nonradiative ${}^2B'_2 \rightarrow {}^2B_2$ transition is a second-order two-phonon process, and as such, it should occur at a much slower rate than the already negligible nonradiative rates.

Calculating the nonradiative rates for the intersystem crossing transitions is beyond the scope of this paper.

XI. OPTICALLY DETECTED MAGNETIC RESONANCE SIGNAL

There have been reports of ODMR signals for defects in h-BN. One of them is known to originate from the V_B^- defect [48], while the origins of the other observed ODMR signals are not established yet [19,49]. Here, we present our results for the ODMR simulation using the model in Fig. 4 for the C_2C_N defect. We used the Lindblad master equation to derive the second-order correlation function $g^{(2)}$ and the ODMR contrast.

The Lindblad master equation is defined as

$$\frac{d}{dt} \rho = \mathcal{L} \rho \equiv -i[H, \rho] + \sum_k \Gamma_k \left(L_k \rho L_k^\dagger - \frac{1}{2} \{L_k L_k^\dagger, \rho\} \right), \quad (22)$$

where \mathcal{L} is the Liouvillian superoperator [30]. The first term of \mathcal{L} gives the unitary time evolution of the density matrix ρ , and the other terms are responsible for the transitions of the system. The operators L_k are called jump operators, and the constants Γ_k are the transition rates. We have used three types of jump operators in our simulation, including operators for optical, nonradiative, and spin transitions.

We simulate a coherent laser pulse to excite the ground doublet state $\{|1\rangle, |2\rangle\}$ to one of the two excited doublet states $\{|3\rangle, |4\rangle\}$ or $\{|5\rangle, |6\rangle\}$. All of these electronic states are spin-1/2 states, and their spin states are split due to an external magnetic field. We also simulate a coherent microwave pulse to probe the ODMR signal by changing its energy around the spin-splitting energy.

If the quartet dark states $\{|7\rangle, |8\rangle, |9\rangle, |10\rangle\}$ do not overlap with the phonon sideband of the first-excited states $\{|3\rangle, |4\rangle\}$, they can act as a metastable manifold during the decay of the second-excited states $\{|5\rangle, |6\rangle\}$. Since we predict that the quartet energy of around 4.1 eV is far above the 1.6 eV of the

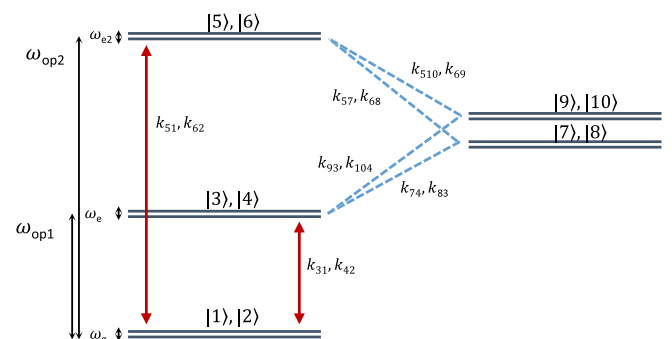


FIG. 4. Our model for ODMR simulation. In this model, the energy spacing between levels, denoted ω_{op1} and ω_{op2} , and optical rates, denoted by the red arrows, are based on DFT calculations and nonradiative rates to and from the metastable states, denoted by blue dashed lines, are approximated by rates from other studies on defects in h-BN. There are also spin splittings due to the external magnetic field, which are denoted by ω_g , ω_e , and ω_{e2} . According to the matrix elements of the spin-orbit and spin-spin of this defect, the dashed lines are spin-dependent transitions which are vital for observing an ODMR signal.

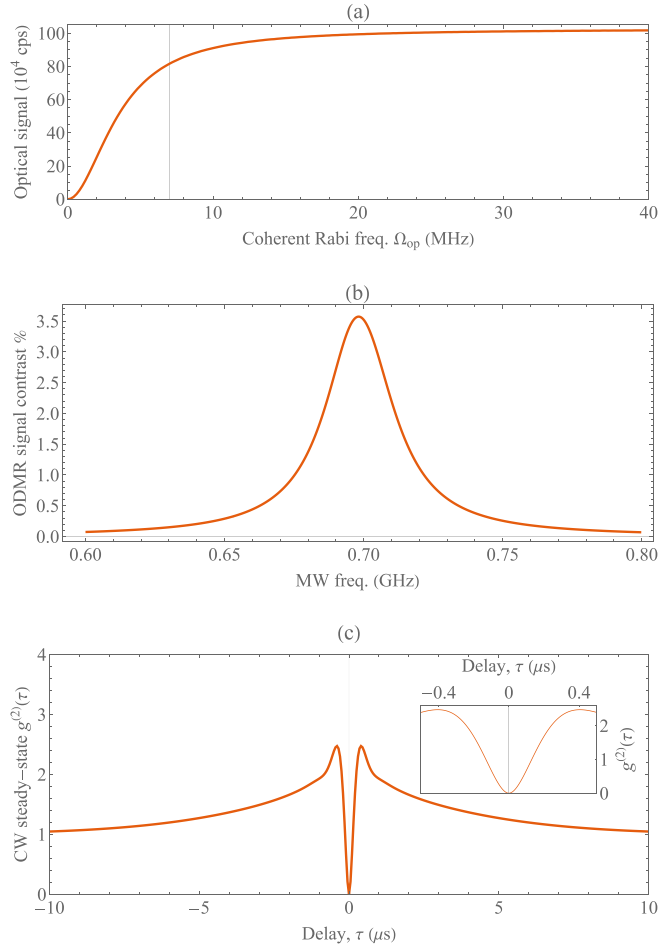


FIG. 5. Results of exciting photons to the second excited doublet state and detecting photon emissions from the same state to the ground state. (a) Optical signal versus coherent Rabi frequency, which shows saturation near 20 MHz. The grid line shows the Rabi frequency that we used for the ODMR signal and the g^2 function. This is the frequency where the optical signal is near 80% of the saturation point. (b) The ODMR signal, which shows 3.5% contrast at 700 MHz MW frequency. (c) The second-order correlation function, which shows significant bunching at microsecond timescales due to the metastable quartet state, and antibunching pattern at $\tau = 0$. Inset shows the same g^2 function for smaller timescales.

first-excited doublet, it is unlikely that there is an overlap with the phonon sideband, which is typically smaller than about 500 meV for defects in h-BN [16]. In addition, the decay to the quartet state and from the quartet state to the first-excited state can depend on the spin, and hence the system could produce an ODMR signal. To see this signal, one should excite the ground-state levels to the second-excited state doublet $\{|5\rangle, |6\rangle\}$, after which a spin-dependent nonradiative transition can occur into the quartet manifold.

The ${}^2B'_2$ state is the most promising candidate for photoexcitation because its energy is very close to the quartet state and, most likely, it will overlap with its phonon sideband, allowing for fast nonradiative transitions to the metastable state. Thus, we restricted the model to the ${}^2B'_2$ level and ignored ${}^2A'_2$ and ${}^2A''_2$ levels because of their high energy. We also ignored

TABLE VI. Parameters used in the ODMR simulation. Ω_{op} is the coherent optical driving Rabi frequency, Ω_{MW} is the coherent microwave driving Rabi frequency, γ_{spin} is the spin relaxation rate, and other parameters are shown in Fig. 4.

Parameter	Value	Parameter	Value
ω_{op2}	4.2 eV	ω_{op1}	1.6 eV
Ω_{op}	7 MHz	Ω_{MW}	13 MHz
k_{51}	6.9 MHz	k_{62}	6.9 MHz
k_{31}	15.5 MHz	k_{42}	15.5 MHz
k_{57}	0.1 MHz	k_{68}	1 MHz
k_{74}	2 MHz	k_{83}	1 MHz
k_{510}	0.95 MHz	k_{69}	0.045 MHz
k_{93}	1.1 MHz	k_{104}	0.11 MHz
ω_g	700 MHz	ω_{e2}	697 MHz
ω_e	703 MHz	γ_{spin}	0.06 MHz

nonradiative transitions related to ${}^2B'_2 \leftrightarrow {}^2A_2$, ${}^2B_2 \leftrightarrow {}^2A_2$, and ${}^4A_2 \leftrightarrow {}^2A_2$ because the energy difference between them is large and it is more likely that the radiative and intersystem crossing transitions will be dominant. Consequently, we need an ultraviolet (UV) laser pulse to excite the ground doublet state to the second excited doublet state. Finally, we detect photons emitted due to the decay of electrons from the second doublet excited state, $\{|5\rangle, |6\rangle\}$, to the ground state, $\{|1\rangle, |2\rangle\}$. UV lasers and detectors will be required to verify our predictions. The equipment and techniques used in ion trap systems could be helpful since some of the ions used in the ion trap systems have a transition in the UV regime, for example, Be^+ (3.96 eV) or Mg^+ (4.43 eV) [50–52].

The results obtained by exciting the ground-state levels directly to the second-excited state and then detecting photon emissions from the same state to the ground state are given in Fig. 5. We have used the optical decay rates from our DFT calculation presented in the previous section. The intersystem crossing rates, metastable decay rates, and spin-relaxation rates for which we see ODMR signals are on the order of magnitude of the rates seen in other defects [53,54], but more calculations are needed to verify if the rates are in the proper range for the $\text{C}_2\text{C}_\text{N}$ defect. In our simulation, we chose the optical Rabi frequency close to the saturation point so that it is not in the resonance regime (Fig. 6). Additionally, the microwave Rabi frequency was chosen such that the ODMR signal had the highest value (Fig. 7). All the parameters used to predict this ODMR signal are given in Table VI.

Some of the parameters used for this simulation were not calculated by *ab initio* calculations. Hence, we probe a bigger space of possible values, keeping the rates close to the rates seen for other defects in h-BN, in order to see how the ODMR signal would change. Varying the parameters used for this model shows that the difference between k_{74} and k_{83} is essential for having an ODMR signal. Based on our calculations for the spin-orbit and the spin-spin interactions, the matrix elements responsible for these transitions are different for the spin up and down. The transition amplitudes are proportional to these matrix elements, allowing the defect to have spin-dependent decay rates from and to the quartet state. The effect of changing k_{74} and k_{83} on the ODMR signal and g^2

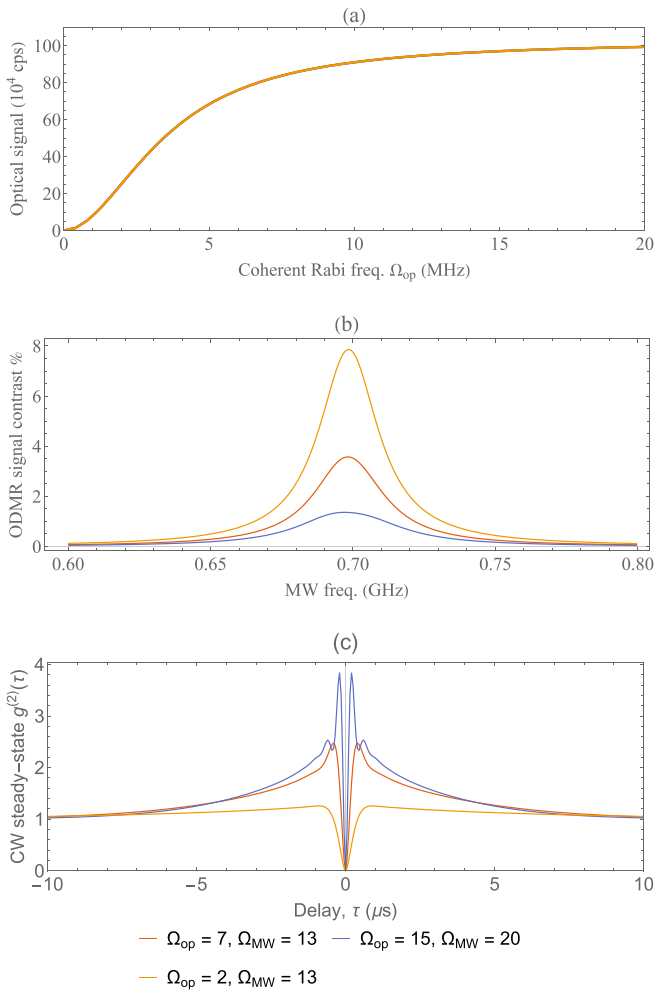


FIG. 6. The effect of changing Ω_{op} on the optical signal, ODMR contrast, and the second-order correlation function. All the variables are in MHz. When the optical Rabi frequency is in the saturation region, e.g., $\Omega_{op} = 15$ MHz, there are oscillations in the $g^{(2)}(\tau)$ function. This might be related to the oscillations seen by Stern *et al.* [19].

correlation function is shown in Fig. 8. Based on the matrix elements of the spin-orbit and spin-spin interactions, the k_{74} and k_{83} rates are related to the k_{93} and k_{104} rates. So changing each of them will affect the other two. More figures are provided in Appendix E. These results show that even for the bigger space of possible transition rates, the ODMR signal of a few percent is viable.

The calculated linewidth of the ODMR signal is due only to the natural or lifetime broadening since we have not included other broadening mechanisms such as the hyperfine interaction in our simulation. However, the most abundant isotopes of nitrogen and boron have nuclear spins of 1 and 3/2, respectively. It has been shown that the hyperfine interaction of the surrounding nuclear spins has a considerable effect on the ODMR linewidth broadening of defects in h-BN (51 MHz for the C_2C_N defect) [24]. As it can be seen in Fig. 8, the linewidth of the ODMR signal due to the natural broadening changes significantly for different nonradiative transition rates, which are still unknown. Therefore, after finding the correct value of the transition rates, it will be crucial to consider hyperfine

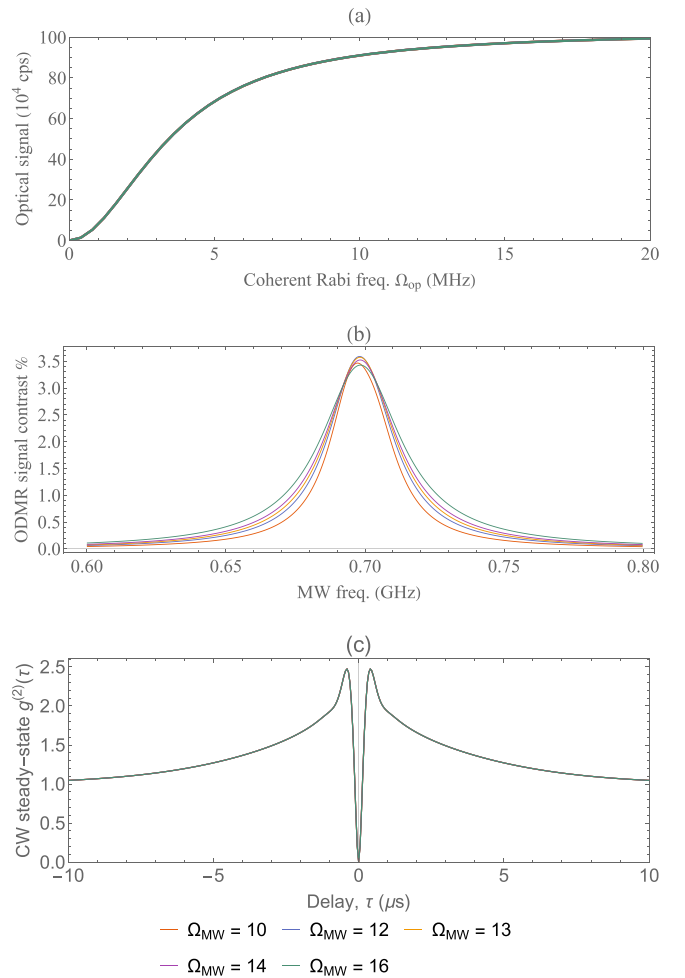


FIG. 7. The effect of changing Ω_{MW} on the optical signal, ODMR contrast, and the second-order correlation function. All the variables are in MHz. It is important to choose Ω_{MW} in a way that the ODMR signal is maximum.

broadening, because the linewidth of the ODMR signal is another parameter that helps identify defects found by the experiment.

XII. COMPUTATIONAL DETAILS

The DFT calculations and postprocessing were performed using the QUANTUM ESPRESSO open-source software package [55]. The calculations utilized a plane-wave basis set with a kinetic-energy cutoff of 350 eV and projector augmented-wave pseudopotentials [56]. All relaxation calculations were performed with a force convergence threshold of 10^{-4} eV/Å. Experimental investigations of point defects in h-BN typically consider multilayer samples; however, it has been shown that DFT calculations result in negligible differences between the electronic structure of defects in single- and multilayer systems [7]. Our supercell consists of 98 atoms and a vacuum separation of 15 Å between layers, corresponding to 7×7 unit cells of monolayer h-BN. The atomic positions and in-plane lattice constant for the pristine h-BN structure were relaxed using the Perdew-Burke-Ernzerhof (PBE) exchange-correlation functional [57]. An in-plane lattice

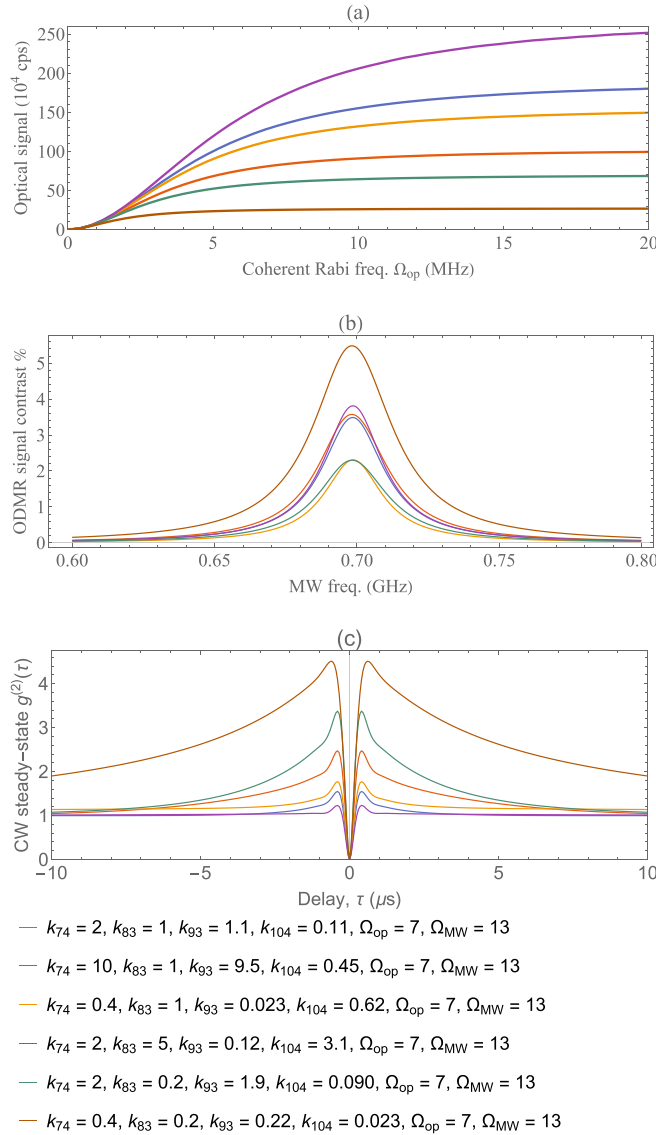


FIG. 8. The effect of changing k_{83} and k_{74} on the optical signal, ODMR contrast, and the second-order correlation function. All the variables are in MHz.

constant of $a = 2.5 \text{ \AA}$ was obtained, consistent with previous findings [58]. The Heyd-Scuseria-Ernzerhof (HSE06) hybrid functional [59] was then used to optimize the direct band gap at the K high-symmetry point [60] to the bulk value of $\approx 6 \text{ eV}$ [17]. A band gap of 5.98 eV was obtained by setting the mixing parameter to 0.32 and fine-tuning the screening parameter to 0.086 \AA^{-1} .

The $\text{C}_2\text{C}_\text{N}$ defect was then added to the hexagonal lattice, the atomic positions were relaxed in-plane, and the ground-state wave functions of the single-particle defect levels were calculated. Next, the single-configuration excited states (2A_2 , 2B_2 , ${}^2B'_2$, and 4A_2) were created using the ΔSCF method [61], and the atomic positions of each excited-state electronic configuration were relaxed in-plane. The transition energies between defect states were calculated by considering the difference in total energies of the structures, obtained via spin-polarized calculations performed within the Γ -point

approximation. The HSE06 functional has been shown to provide accurate results for defects in h-BN which exhibit low correlation and charge transfer, and as such, it is expected that the error in the DFT calculations of the single-configuration states is on the order of 0.1 eV [22,62]. The remaining states of interest (${}^2A'_2$ and ${}^2A''_2$) are multiconfiguration states which cannot be modeled in the DFT calculations using the ΔSCF method. Rough estimates for the corresponding transition energies were obtained following the method of Ref. [42,63], making use of the single-configuration states $|bab'\rangle$, $|bab'\rangle$, and $|b\bar{a}b'\rangle$ which were created within the ΔSCF procedure (see Appendix D for detailed calculations).

Reference [64] investigates the $\text{C}_2\text{C}_\text{N}$ defect. A difference between this work and Ref. [64] can be seen in the positioning of the single-electron states with respect to the conduction and valence bands. The electronic calculations of Ref. [64] were performed within the GW approximation, which can impact both the position and size of the band gap. We note, however, that relative spacing and positions of the defect state energies found in our work are consistent with the findings of both Refs. [22] and [24].

XIII. CONCLUSION

We have used group theory and DFT calculations to find the electronic structure and transitions of the $\text{C}_2\text{C}_\text{N}$ defect in 2D h-BN. The results are summarized in Fig. 3(a), which shows that there are several radiative transitions together with spin-orbit and spin-spin assisted nonradiative transitions. Also, the spin-spin interaction causes a splitting between quartet states 4A_2 . We studied the effect of an external magnetic field and found that, in the presence of an external magnetic field perpendicular to the plane, there is an anticrossing between the states of the quartet manifold. We also looked at the ground-state hyperfine interactions, which can be helpful in future studies. Additionally, we calculated the radiative rates and some of the nonradiative rates using DFT. Finally, we simulated the system using the Lindblad master equation. Although our results indicate that it is unlikely for the $\text{C}_2\text{C}_\text{N}$ defect to be responsible for the ODMR signals that have been reported so far, we show that it could be possible to see an ODMR signal contrast of $\approx 3.5\%$ for the configuration discussed in the text. Some of the nonradiative rates of the $\text{C}_2\text{C}_\text{N}$ are unknown. Hence, we looked at the ODMR signal in a subspace of the possible rates where these variables are close to the reported values from other defects in h-BN and show that an ODMR signal of a few percent is still viable. Besides the ODMR signal contrast, the ODMR linewidth would also help identify this defect in experimental data. Thus, in future research it will be essential to determine both the unknown nonradiative rates and the hyperfine broadening, which has a significant effect. In conclusion, the properties of the defect that we considered are essential for future applications, e.g., for quantum networks and quantum sensing.

ACKNOWLEDGMENTS

We thank Igor Aharonovich for valuable discussions. This work was supported by the Natural Sciences and Engineering Research Council (NSERC) of Canada through its Discovery

Grant and Strategic Project Grants Programs, the Alberta Major Innovation Fund Quantum Technology project, Compute Canada, and the Advanced Research Computing (ARC) IT team of the University of Calgary.

APPENDIX A: MATRIX ELEMENTS OF THE HAMILTONIAN

In this section, we provide the matrix elements of the interactions discussed in the main text.

1. Spin-orbit interaction

The matrix elements of the spin-orbit interaction are given below, where the variables λ , and λ' are defined as

$$\lambda = \langle a|l^{(y)}|b\rangle, \quad \lambda' = \langle b'|l^{(y)}|a\rangle. \quad (A1)$$

$$H_{so} = \frac{i}{2}$$

$$\times \begin{pmatrix} \mathcal{A}_{+1/2}^{0,d} & \mathcal{A}_{-1/2}^{0,d} & \mathcal{B}_{+1/2}^{1,d} & \mathcal{B}_{-1/2}^{1,d} & \mathcal{B}_{+1/2}^{2,d} & \mathcal{B}_{-1/2}^{2,d} & \mathcal{A}_{+1/2}^{3,q} & \mathcal{A}_{-1/2}^{3,q} & \mathcal{A}_{+3/2}^{3,q} & \mathcal{A}_{-3/2}^{3,q} & \mathcal{A}_{+1/2}^{3,d'} & \mathcal{A}_{-1/2}^{3,d'} & \mathcal{A}_{+1/2}^{3,d''} & \mathcal{A}_{-1/2}^{3,d''} \\ \mathcal{A}_{+1/2}^{0,d} & 0 & & & & & & & & & & & & & \\ \mathcal{A}_{-1/2}^{0,d} & 0 & 0 & & & & & & & & & & & & \\ \mathcal{B}_{+1/2}^{1,d} & 0 & -\lambda & 0 & & & & & & & & & & & \\ \mathcal{B}_{-1/2}^{1,d} & \lambda & 0 & 0 & 0 & & & & & & & & & & \\ \mathcal{B}_{+1/2}^{2,d} & 0 & -\lambda' & 0 & 0 & 0 & & & & & & & & & \\ \mathcal{B}_{-1/2}^{2,d} & \lambda' & 0 & 0 & 0 & 0 & 0 & & & & & & & & \\ \mathcal{A}_{+1/2}^{3,q} & 0 & 0 & 0 & -\lambda'/\sqrt{3} & 0 & -\lambda/\sqrt{3} & 0 & & & & & & & \\ \mathcal{A}_{-1/2}^{3,q} & 0 & 0 & -\lambda'/\sqrt{3} & 0 & -\lambda/\sqrt{3} & 0 & 0 & 0 & & & & & & \\ \mathcal{A}_{+3/2}^{3,q} & 0 & 0 & -\lambda' & 0 & -\lambda & 0 & 0 & 0 & 0 & & & & & \\ \mathcal{A}_{-3/2}^{3,q} & 0 & 0 & 0 & -\lambda' & 0 & -\lambda & 0 & 0 & 0 & 0 & & & & \\ \mathcal{A}_{+1/2}^{3,d'} & 0 & 0 & 0 & -\lambda'/2\sqrt{3} & 0 & \lambda/\sqrt{3} & 0 & 0 & 0 & 0 & 0 & & & \\ \mathcal{A}_{-1/2}^{3,d'} & 0 & 0 & -\lambda'/2\sqrt{3} & 0 & \lambda/\sqrt{3} & 0 & 0 & 0 & 0 & 0 & 0 & 0 & & \\ \mathcal{A}_{+1/2}^{3,d''} & 0 & 0 & 0 & \lambda'/2 & 0 & 0 & 0 & 0 & 0 & 0 & 0 & 0 & 0 & \\ \mathcal{A}_{-1/2}^{3,d''} & 0 & 0 & \lambda'/2 & 0 & 0 & 0 & 0 & 0 & 0 & 0 & 0 & 0 & 0 & 0. \end{pmatrix} \quad (A2)$$

2. Spin-Spin Interaction

We can see from Table III that the only elements of D that transform as IRs A_1 and B_1 would yield nonzero values. These are $\hat{D}^{A_1} = \{\hat{D}_{xx}, \hat{D}_{yy}, \hat{D}_{zz}\}$ and $\hat{D}^{B_1} = (\hat{D}_{xz} + \hat{D}_{zx})/2$. In this interaction, we have the product of two rank-two tensors (see Table VII). This product can be reduced to a sum of rank four, three, two, one, and zero irreducible tensor operators. Nevertheless, here we need a compound tensor operator of rank zero. This tensor product is given by the equation below [34]:

$$[\hat{s}^{(2)} \otimes \hat{D}^{(2)}]_0^{(0)} = \frac{1}{\sqrt{5}} \sum_{q=-2}^{+2} (-1)^{2-q} \hat{s}_{-q}^{(2)} \hat{D}_q^{(2)}. \quad (A3)$$

TABLE VII. Second-rank spin tensor.

Compound tensor	q	Spherical component
$\{\hat{s}_i^{(1)} \otimes \hat{s}_j^{(1)}\}_q^{(2)}$	+2	$\hat{s}_{i+1}^{(1)} \hat{s}_{j+1}^{(1)}$
	+1	$(\hat{s}_{i+1}^{(1)} \hat{s}_{j,0}^{(1)} + \hat{s}_{i,0}^{(1)} \hat{s}_{j+1}^{(1)})/\sqrt{2}$
	0	$\frac{1}{\sqrt{6}}(\hat{s}_{i,-1}^{(1)} \hat{s}_{j+1}^{(1)} + 2\hat{s}_{i,0}^{(1)} \hat{s}_{j,0}^{(1)} + \hat{s}_{i+1}^{(1)} \hat{s}_{j,-1}^{(1)})$
	-1	$(\hat{s}_{i,-1}^{(1)} \hat{s}_{j,0}^{(1)} + \hat{s}_{i,0}^{(1)} \hat{s}_{j,-1}^{(1)})/\sqrt{2}$
	-2	$\hat{s}_{i,-1}^{(1)} \hat{s}_{j,-1}^{(1)}$

To use Eq. (A3), we need the spherical components of \hat{D} . Spherical and Cartesian components of \hat{D} are related by the equations below:

$$\begin{aligned} \hat{D}_{\pm 2}^{(2)} &= (\hat{D}_{xx}^{(2)} - \hat{D}_{yy}^{(2)} \pm 2i\hat{D}_{xy}^{(2)})/\sqrt{2}, \\ \hat{D}_{\pm 1}^{(2)} &= \mp(\hat{D}_{xz}^{(2)} \pm i\hat{D}_{yz}^{(2)}), \\ \hat{D}_0^{(2)} &= (2\hat{D}_{zz}^{(2)} - \hat{D}_{xx}^{(2)} - \hat{D}_{yy}^{(2)})/\sqrt{6}. \end{aligned} \quad (A4)$$

The components of $\hat{s}^{(1)}$ in the notation of spherical tensor operators are given by

$$\begin{aligned} \hat{s}_{+1}^{(1)} &= -\frac{1}{\sqrt{2}}(\hat{s}_x + i\hat{s}_y), \quad \hat{s}_0^{(1)} = \hat{s}_z, \\ \hat{s}_{-1}^{(1)} &= \frac{1}{\sqrt{2}}(\hat{s}_x - i\hat{s}_y), \quad \hat{s}_{+1}^{(1)} \left| -\frac{1}{2} \right\rangle = -\frac{1}{\sqrt{2}} \left| +\frac{1}{2} \right\rangle, \\ \hat{s}_{-1}^{(1)} \left| +\frac{1}{2} \right\rangle &= \frac{1}{\sqrt{2}} \left| -\frac{1}{2} \right\rangle. \end{aligned} \quad (A5)$$

Now that we have all the preliminary tools, we will derive the matrix elements. For the elements in the form of $\langle \mathcal{A}|H_{ss}|\mathcal{A}'\rangle$ and $\langle \mathcal{B}|H_{ss}|\mathcal{B}'\rangle$, according to Table III, only the parts of H_{ss} that transform as IR A_1 would yield nonzero

values. $|\mathcal{A}\rangle$ and $|\mathcal{A}'\rangle$ can be any of states in Table II that transform as IR A_2 and similarly $|\mathcal{B}\rangle$ and $|\mathcal{B}'\rangle$ can be any of states in Table II that transform as IR B_2 . $\{\hat{D}_{xx}, \hat{D}_{yy}, \hat{D}_{zz}\}$ are the only components of \hat{D} that transform as IR A_1 . In the spherical tensor form, \hat{D}_0 transforms as IR A_1 and first two components of $\hat{D}_{\pm 2}$ also transform as IR A_1 . Therefore, just \hat{D}_0 , and $\hat{D}_{\pm 2}$ contribute to nonzero values. At last, according to Eq. (A3), $\Delta S \in \{0, \pm 2\}$. Similarly, for $\langle \mathcal{A} | H_{ss} | \mathcal{B} \rangle$ according to Table III, only the parts of H_{ss} that transform as IR B_1 would yield nonzero values. $\{\hat{D}_{xz}, \hat{D}_{zx}\}$ are the only components of

\hat{D} that transform as IR B_1 . Therefore, just $\hat{D}_{\pm 1}$ contributes to nonzero values. For these matrix elements, according to Eq. (A3), we have $\Delta S \in \{\pm 1\}$,

$$\left. \begin{aligned} \langle \mathcal{A} | H_{ss} | \mathcal{A}' \rangle \\ \langle \mathcal{B} | H_{ss} | \mathcal{B}' \rangle \end{aligned} \right\} \rightarrow A_1 \rightarrow \hat{D}_0, \quad \hat{D}_{\pm 2} \rightarrow \Delta S \in \{0, \pm 2\},$$

$$\langle \mathcal{A} | H_{ss} | \mathcal{B} \rangle \rightarrow B_1 \rightarrow \hat{D}_{\pm 1} \rightarrow \Delta S \in \{\pm 1\}. \quad (\text{A6})$$

After doing all the calculations, we get the matrix elements for the spin-spin interaction, shown below:

$$H_{ss} = \frac{\mu_0 \gamma_e^2 \hbar^2}{16\pi} \times \begin{pmatrix} \mathcal{A}_{+1/2}^{0,d} & \mathcal{A}_{-1/2}^{0,d} & \mathcal{B}_{+1/2}^{1,d} & \mathcal{B}_{-1/2}^{1,d} & \mathcal{B}_{+1/2}^{2,d} & \mathcal{B}_{-1/2}^{2,d} & \mathcal{A}_{+1/2}^{3,q} & \mathcal{A}_{-1/2}^{3,q} & \mathcal{A}_{+3/2}^{3,q} & \mathcal{A}_{-3/2}^{3,q} & \mathcal{A}_{+1/2}^{3,d'} & \mathcal{A}_{-1/2}^{3,d'} & \mathcal{A}_{+1/2}^{3,d''} & \mathcal{A}_{-1/2}^{3,d''} \\ \mathcal{A}_{+1/2}^{0,d} & 0 & & & & & & & & & & & & & \\ \mathcal{A}_{-1/2}^{0,d} & 0 & 0 & & & & & & & & & & & & \\ \mathcal{B}_{+1/2}^{1,d} & 0 & 0 & 0 & & & & & & & & & & & \\ \mathcal{B}_{-1/2}^{1,d} & 0 & 0 & 0 & 0 & & & & & & & & & & \\ \mathcal{B}_{+1/2}^{2,d} & 0 & 0 & 0 & 0 & 0 & & & & & & & & & \\ \mathcal{B}_{-1/2}^{2,d} & 0 & 0 & 0 & 0 & 0 & 0 & & & & & & & & \\ \mathcal{A}_{+1/2}^{3,q} & \mathcal{E}_1 & 0 & 0 & -\mathcal{F}_1 & 0 & \mathcal{F}_2 & -\mathcal{D}_0 & & & & & & & \\ \mathcal{A}_{-1/2}^{3,q} & 0 & -\mathcal{E}_1 & \mathcal{F}_1 & 0 & -\mathcal{F}_2 & 0 & 0 & -\mathcal{D}_0 & & & & & & \\ \mathcal{A}_{+3/2}^{3,q} & 0 & -\mathcal{E}_2 & \frac{-1}{\sqrt{3}}\mathcal{F}_1 & 0 & \frac{1}{\sqrt{3}}\mathcal{F}_2 & 0 & 0 & \mathcal{E}_3 & \mathcal{D}_0 & & & & & \\ \mathcal{A}_{-3/2}^{3,q} & \mathcal{E}_2 & 0 & 0 & \frac{1}{\sqrt{3}}\mathcal{F}_1 & 0 & \frac{-1}{\sqrt{3}}\mathcal{F}_2 & \mathcal{E}_3 & 0 & 0 & \mathcal{D}_0 & & & & \\ \mathcal{A}_{+1/2}^{3,d'} & 0 & 0 & 0 & -\mathcal{G} & 0 & 0 & -\mathcal{H} & 0 & 0 & \mathcal{K}^* & 0 & & & \\ \mathcal{A}_{-1/2}^{3,d'} & 0 & 0 & -\mathcal{G} & 0 & 0 & 0 & 0 & -\mathcal{H} & \mathcal{K}^* & 0 & 0 & 0 & & \\ \mathcal{A}_{+1/2}^{3,d''} & 0 & 0 & 0 & 0 & 0 & 0 & \mathcal{I} & 0 & 0 & \mathcal{L}^* & \mathcal{J} & 0 & 0 & \\ \mathcal{A}_{-1/2}^{3,d''} & 0 & 0 & 0 & 0 & 0 & 0 & 0 & \mathcal{I} & \mathcal{L}^* & 0 & 0 & \mathcal{J} & 0 & 0. \end{pmatrix} \quad (\text{A7})$$

The matrix elements used above are defined as

$$\mathcal{D}_0 = \frac{1}{2\sqrt{5}} (\langle bb' - b'b | \hat{D}_{zz}^{(2)} | bb' - b'b \rangle + \langle ba - ab | \hat{D}_{zz}^{(2)} | ba - ab \rangle + \langle ab' - b'a | \hat{D}_{zz}^{(2)} | ab' - b'a \rangle),$$

$$\mathcal{E}_1 = \frac{1}{15} \langle ab' - b'a | \hat{D}_{zz}^{(2)} | ab - ba \rangle, \quad \mathcal{E}_2 = \frac{1}{10} \langle ab' - b'a | \hat{D}_{xx}^{(2)} - \hat{D}_{yy}^{(2)} | ab - ba \rangle,$$

$$\mathcal{E}_3 = \frac{1}{\sqrt{30}} (\langle ab' - b'a | \hat{D}_{xx}^{(2)} - \hat{D}_{yy}^{(2)} | ab' - b'a \rangle + \langle bb' - b'b | \hat{D}_{xx}^{(2)} - \hat{D}_{yy}^{(2)} | bb' - b'b \rangle + \langle ab - ba | \hat{D}_{xx}^{(2)} - \hat{D}_{yy}^{(2)} | ab - ba \rangle),$$

$$\mathcal{F}_1 = \frac{\sqrt{3}}{2\sqrt{5}} \langle bb' - b'b | \hat{D}_{xz}^{(2)} | ab - ba \rangle, \quad \mathcal{F}_2 = \frac{\sqrt{3}}{2\sqrt{5}} \langle ab' - b'a | \hat{D}_{xz}^{(2)} | bb' - b'b \rangle, \quad (\text{A8})$$

$$\mathcal{G} = \frac{1}{\sqrt{30}} \langle bb' - b'b | \hat{D}_{xz}^{(2)} | ba - ab \rangle,$$

$$\mathcal{H} = \frac{1}{6\sqrt{10}} \{ \langle bb' - b'b | \hat{D}_{zz}^{(2)} | bb' - b'b \rangle + \langle ba - ab | \hat{D}_{zz}^{(2)} | ba - ab \rangle - 2 \langle ab' - b'a | \hat{D}_{zz}^{(2)} | ab' - b'a \rangle \},$$

$$\mathcal{I} = \frac{\sqrt{3}}{2\sqrt{10}} \{ - \langle bb' - b'b | \hat{D}_{zz}^{(2)} | bb' - b'b \rangle + \langle ab' - b'a | \hat{D}_{zz}^{(2)} | ab' - b'a \rangle \}, \quad \mathcal{J} = - \frac{1}{2\sqrt{15}} \langle ab' - b'a | \hat{D}_{zz}^{(2)} | ab' - b'a \rangle,$$

$$\mathcal{K} = \frac{1}{2\sqrt{15}} \{ + \langle ab' - b'a | (\hat{D}_{xx}^{(2)} - \hat{D}_{yy}^{(2)}) | ab' - b'a \rangle + \langle bb' - b'b | (\hat{D}_{xx}^{(2)} - \hat{D}_{yy}^{(2)}) | bb' - b'b \rangle - 2 \langle ba - ab | (\hat{D}_{xx}^{(2)} - \hat{D}_{yy}^{(2)}) | ba - ab \rangle \},$$

$$\mathcal{L} = \frac{1}{2\sqrt{5}} \{ - \langle ab' - b'a | (\hat{D}_{xx}^{(2)} - \hat{D}_{yy}^{(2)}) | ab' - b'a \rangle + \langle bb' - b'b | (\hat{D}_{xx}^{(2)} - \hat{D}_{yy}^{(2)}) | bb' - b'b \rangle \}. \quad (\text{A9})$$

3. Dipole transitions

The dipole-allowed transition rates would be proportional to the values defined below:

$$\begin{aligned} \mu_x &= eE_x \langle a|x|b \rangle, \quad \mu'_x = eE_x \langle a|x|b' \rangle, \quad \mu_{z,0} = eE_z \{ \langle b|z|b \rangle + \langle a|z|a \rangle + \langle b'|z|b' \rangle \}, \quad \mu_{z,1} = eE_z \{ 2\langle b|z|b \rangle + \langle a|z|a \rangle \}, \\ \mu_{z,2} &= eE_z \{ \langle b|z|b \rangle + 2\langle a|z|a \rangle \}, \quad \mu_{z,3} = eE_z \{ 2\langle b|z|b \rangle + \langle b'|z|b' \rangle \}, \quad \mu'_z = eE_z \langle b|z|b' \rangle. \end{aligned} \quad (\text{A10})$$

Furthermore, the matrix elements are as shown below:

$$H_{\text{dipole}} = \begin{pmatrix} \mathcal{A}_{+1/2}^{0,d} & \mathcal{A}_{-1/2}^{0,d} & \mathcal{B}_{+1/2}^{1,d} & \mathcal{B}_{-1/2}^{1,d} & \mathcal{B}_{+1/2}^{2,d} & \mathcal{B}_{-1/2}^{2,d} & \mathcal{A}_{+1/2}^{3,q} & \mathcal{A}_{-1/2}^{3,q} & \mathcal{A}_{+3/2}^{3,q} & \mathcal{A}_{-3/2}^{3,q} & \mathcal{A}_{+1/2}^{3,d'} & \mathcal{A}_{-1/2}^{3,d'} & \mathcal{A}_{+1/2}^{3,d''} & \mathcal{A}_{-1/2}^{3,d''} \\ \mathcal{A}_{+1/2}^{0,d} & \mu_{z,1} & & & & & & & & & & & & \\ \mathcal{A}_{-1/2}^{0,d} & 0 & \mu_{z,1} & & & & & & & & & & & \\ \mathcal{B}_{+1/2}^{1,d} & -\mu_x & 0 & \mu_{z,2} & & & & & & & & & & \\ \mathcal{B}_{-1/2}^{1,d} & 0 & \mu_x & 0 & \mu_{z,2} & & & & & & & & & \\ \mathcal{B}_{+1/2}^{2,d} & \mu_x^* & 0 & 0 & 0 & \mu_{z,3} & & & & & & & & \\ \mathcal{B}_{-1/2}^{2,d} & 0 & \mu_x^* & 0 & 0 & 0 & \mu_{z,3} & & & & & & & \\ \mathcal{A}_{+1/2}^{3,q} & 0 & 0 & 0 & 0 & 0 & 0 & \mu_{z,0} & & & & & & \\ = \mathcal{A}_{-1/2}^{3,q} & 0 & 0 & 0 & 0 & 0 & 0 & 0 & \mu_{z,0} & & & & & \\ \mathcal{A}_{+3/2}^{3,q} & 0 & 0 & 0 & 0 & 0 & 0 & 0 & 0 & \mu_{z,0} & & & & \\ \mathcal{A}_{-3/2}^{3,q} & 0 & 0 & 0 & 0 & 0 & 0 & 0 & 0 & 0 & \mu_{z,0} & & & \\ \mathcal{A}_{+1/2}^{3,d'} & \frac{3\mu_x^*}{\sqrt{6}} & 0 & -\frac{3\mu_x^*}{\sqrt{6}} & 0 & 0 & 0 & 0 & 0 & 0 & 0 & 0 & & \\ \mathcal{A}_{-1/2}^{3,d'} & 0 & \frac{3\mu_x^*}{\sqrt{6}} & 0 & -\frac{3\mu_x^*}{\sqrt{6}} & 0 & 0 & 0 & 0 & 0 & 0 & 0 & & \\ \mathcal{A}_{+1/2}^{3,d''} & -\frac{\mu_z^*}{\sqrt{2}} & 0 & -\frac{\mu_z^*}{\sqrt{2}} & 0 & \frac{2\mu_x'}{\sqrt{2}} & 0 & 0 & 0 & 0 & 0 & 0 & 0 & \\ \mathcal{A}_{-1/2}^{3,d''} & 0 & -\frac{\mu_z^*}{\sqrt{2}} & 0 & -\frac{\mu_z^*}{\sqrt{2}} & 0 & \frac{2\mu_x'}{\sqrt{2}} & 0 & 0 & 0 & 0 & 0 & 0 & 0 \end{pmatrix} \quad (\text{A11})$$

APPENDIX B: MAGNETIC INTERACTION

We define the following values for single molecular orbitals:

$$\eta = \langle a|l_y|b \rangle, \quad \eta' = \langle a|l_y|b' \rangle, \quad (\text{B1})$$

$$H_B = \frac{\gamma_e \hbar}{2}$$

$$\times \begin{pmatrix} \mathcal{A}_{+1/2}^{0,d} & \mathcal{A}_{-1/2}^{0,d} & \mathcal{B}_{+1/2}^{1,d} & \mathcal{B}_{-1/2}^{1,d} & \mathcal{B}_{+1/2}^{2,d} & \mathcal{B}_{-1/2}^{2,d} & \mathcal{A}_{+1/2}^{3,q} & \mathcal{A}_{-1/2}^{3,q} & \mathcal{A}_{+3/2}^{3,q} & \mathcal{A}_{-3/2}^{3,q} \\ \mathcal{A}_{+1/2}^{0,d} & B_z & & & & & & & & & & & & \\ \mathcal{A}_{-1/2}^{0,d} & (B_x + iB_y) & -B_z & & & & & & & & & & & \\ \mathcal{B}_{+1/2}^{1,d} & \frac{2B_y}{g_e} \eta & 0 & B_z & & & & & & & & & & \\ \mathcal{B}_{-1/2}^{1,d} & 0 & \frac{2B_y}{g_e} \eta & (B_x + iB_y) & -B_z & & & & & & & & & \\ \times \mathcal{B}_{+1/2}^{2,d} & \frac{2B_y}{g_e} \eta^* & 0 & 0 & 0 & B_z & & & & & & & & \\ \mathcal{B}_{-1/2}^{2,d} & 0 & \frac{2B_y}{g_e} \eta^* & 0 & 0 & (B_x + iB_y) & -B_z & & & & & & & \\ \mathcal{A}_{+1/2}^{3,q} & 0 & 0 & 0 & 0 & 0 & 0 & B_z & & & & & & \\ \mathcal{A}_{-1/2}^{3,q} & 0 & 0 & 0 & 0 & 0 & 0 & 2(B_x + iB_y) & -B_z & & & & & \\ \mathcal{A}_{+3/2}^{3,q} & 0 & 0 & 0 & 0 & 0 & 0 & \sqrt{3}(B_x - iB_y) & 0 & 3B_z & & & & \\ \mathcal{A}_{-3/2}^{3,q} & 0 & 0 & 0 & 0 & 0 & 0 & 0 & \sqrt{3}(B_x + iB_y) & 0 & -3B_z & & & \end{pmatrix} \quad (\text{B2})$$

TABLE VIII. Eigensystem of the hyperfine interaction for the ground state in Eq. (C2). Eigenvalues should be multiplied by $-\frac{C_{\text{mhf}}}{12\sqrt{5}}$.

Hyperfine interaction		
Eigenvalues	Eigenstates	Eigenstates in primary basis
$-(1 + \sqrt{2})G_0$	$(1 + \sqrt{2})\Psi_2 + \Psi_4$	$(1 + \sqrt{2}) b\bar{b}a-\rangle + b\bar{b}\bar{a}+\rangle$
$-(1 - \sqrt{2})G_0$	$(1 - \sqrt{2})\Psi_2 + \Psi_4$	$- b\bar{b}a-\rangle + (1 + \sqrt{2}) b\bar{b}\bar{a}+\rangle$
$G_0 - 3\sqrt{2}G_1$	$\Psi_1 + \Psi_3$	$ b\bar{b}a+\rangle + b\bar{b}\bar{a}-\rangle$
$G_0 + 3\sqrt{2}G_1$	$-\Psi_1 + \Psi_3$	$- b\bar{b}a+\rangle + b\bar{b}\bar{a}-\rangle$

APPENDIX C: HYPERFINE INTERACTION

We can write the hyperfine interaction in the form of spherical components as below:

$$\begin{aligned} \hat{V}_{\text{mhf}} &= -C_{\text{mhf}} \sum_i [\hat{J}_i^{(2)} \otimes \hat{A}_i^{(2)}]^{(0)} \\ &= -\frac{C_{\text{mhf}}}{\sqrt{5}} \sum_i \sum_{q=-2}^{q=+2} (-1)^{2-q} J_{i,-q}^{(2)} A_{i,+q}^{(2)}. \end{aligned} \quad (\text{C1})$$

After doing the calculations, we end up with the following Hamiltonian for the ground state (cf. Table VIII):

$$V_{\text{mhf}} = -\frac{C_{\text{mhf}}}{12\sqrt{5}} \begin{pmatrix} \Psi_1 & \Psi_2 & \Psi_3 & \Psi_4 \\ \Psi_1 & G_0 & 0 & 0 \\ \Psi_2 & 0 & -2G_0 & 0 \\ \Psi_3 & -3\sqrt{2}G_1 & 0 & G_0 \\ \Psi_4 & 0 & -G_0 & 0 \end{pmatrix}, \quad (\text{C2})$$

where

$$\begin{aligned} G_0 &= \langle a | (2A_{zz}^{(2)} - A_{xx}^{(2)} - A_{yy}^{(2)}) | a \rangle, \\ G_1 &= \langle a | (A_{xx}^{(2)} - A_{yy}^{(2)}) | a \rangle. \end{aligned} \quad (\text{C3})$$

APPENDIX D: CALCULATIONS OF THE MULTICONFIGURATION STATES

Here, we use the single-configuration states to estimate the energies of the corresponding multiconfiguration states. We only look at the spin-up quartet and doublet states, but the spin-down calculations are similar. We start with quartet and doublet superposition states:

$$\begin{aligned} |\Psi_q\rangle &= \frac{1}{\sqrt{3}} |\beta\alpha\alpha + \alpha\beta\alpha + \alpha\alpha\beta\rangle, \\ |\Psi_{d'}\rangle &= \frac{1}{\sqrt{6}} |\beta\alpha\alpha + \alpha\beta\alpha - 2\alpha\alpha\beta\rangle, \\ |\Psi_{d''}\rangle &= \frac{1}{\sqrt{2}} |-\beta\alpha\alpha + \alpha\beta\alpha\rangle. \end{aligned} \quad (\text{D1})$$

Since $|\alpha\alpha\alpha\rangle$ is also a quartet state, we have $E_q \equiv E[|\Psi_q\rangle] = E[|\alpha\alpha\alpha\rangle]$. By using the equation

$$\frac{1}{\sqrt{3}} (|\Psi_q\rangle - \sqrt{2}|\Psi_{d'}\rangle) = |\alpha\alpha\beta\rangle, \quad (\text{D2})$$

 TABLE IX. Electron-spin configurations corresponding to $|bab'\rangle$ and their energies obtained from DFT. α (β) represents spin up (down).

State	Energy
$ \alpha\alpha\beta\rangle$	4.7 eV
$ \beta\alpha\alpha\rangle$	5.4 eV
$ \alpha\beta\alpha\rangle$	5.5 eV

we have $E[|\alpha\alpha\beta\rangle] = \frac{1}{3}(E_q + 2E[|\Psi_{d'}\rangle])$. Thus, $E_{d'} \equiv E[|\Psi_{d'}\rangle] = (3E[|\alpha\alpha\beta\rangle] - E_q)/2$. Based on our DFT calculations in Table IX, $E[|\alpha\alpha\beta\rangle] = 4.7$ eV and $E_q = 4.1$ eV,

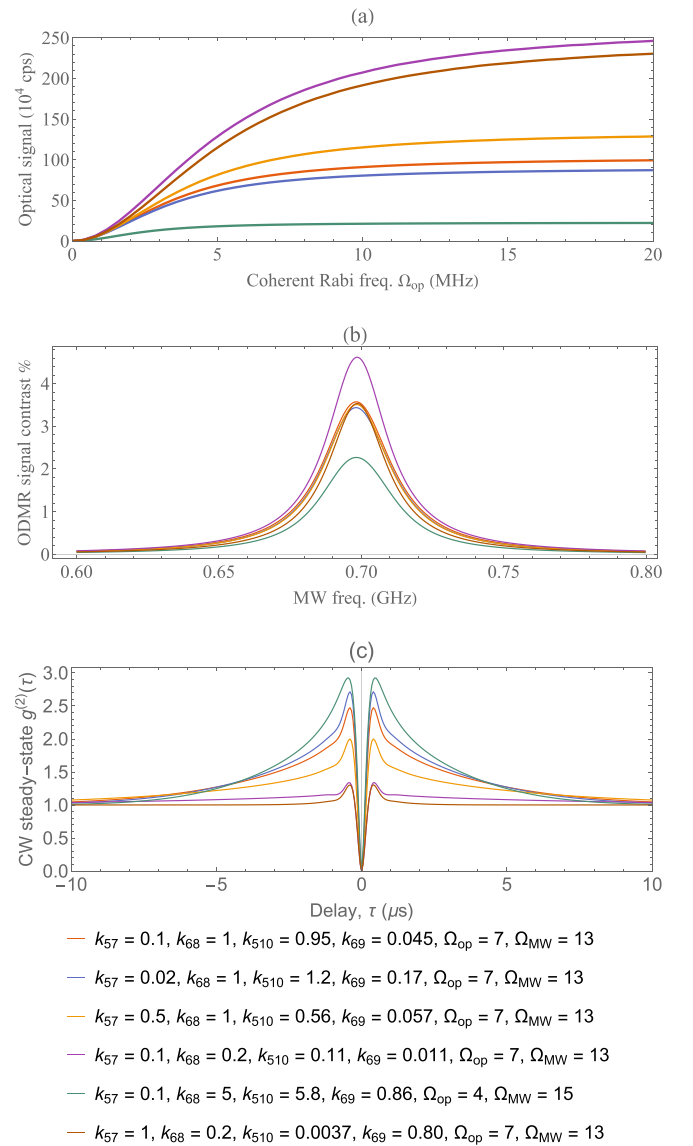


FIG. 9. The effect of changing k_{57} and k_{68} on the optical signal, ODMR contrast, and the second-order correlation function. All the variables are in MHz. Based on the matrix elements of the spin-orbit and spin-spin interactions, the k_{57} and k_{68} rates are related to the k_{510} and k_{69} rates. So changing each of them will affect the other two.

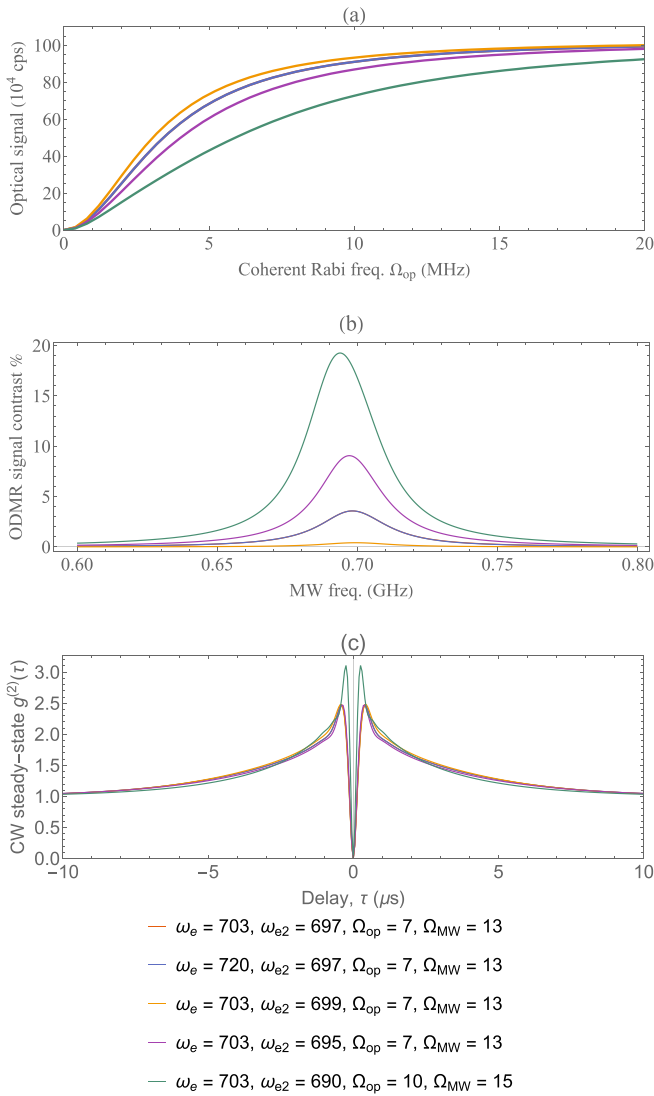


FIG. 10. The effect of changing ω_e and ω_{e2} on the optical signal, ODMR contrast, and the second-order correlation function. All the variables are in MHz.

which implies that $E_{d'} = (3 \times 4.7 - 4.1)/2 = 5$ eV. Next, we define auxiliary state ϕ :

$$\begin{aligned}
 |\phi\rangle &\equiv \frac{1}{2\sqrt{3}}(\sqrt{3}|\Psi_{d'}\rangle + 3|\Psi_{d''}\rangle) \\
 &= \frac{1}{2\sqrt{6}}| -2\beta\alpha\alpha + 4\alpha\beta\alpha - 2\alpha\alpha\beta\rangle \\
 &= \frac{1}{\sqrt{6}}| -\beta\alpha\alpha + 2\alpha\beta\alpha - \alpha\alpha\beta\rangle. \quad (D3)
 \end{aligned}$$

By using this auxiliary state, we show that

$$\frac{1}{\sqrt{3}}(|\Psi_q\rangle + \sqrt{2}|\phi\rangle) = |\alpha\beta\alpha\rangle. \quad (D4)$$

Similar to previous calculation, we can show that

$$\begin{aligned}
 E[|\alpha\beta\alpha\rangle] &= \frac{1}{3}(E_q + 2E_\phi) \\
 &= \frac{1}{3}\{E_q + \frac{1}{6}(3E_{d'} + 9E_{d''} + 3\sqrt{3}\langle\Psi_{d'}|H|\Psi_{d''}\rangle)\}
 \end{aligned}$$

$$\begin{aligned}
 &+ 3\sqrt{3}\langle\Psi_{d'}|H|\Psi_{d''}\rangle\} \\
 &= \frac{1}{6}\{2E_q + E_{d'} + 3E_{d''}\}. \quad (D5)
 \end{aligned}$$

Therefore, we can calculate $E_{d''}$ as below:

$$\begin{aligned}
 E_{d''} &= \frac{1}{3}\{6E[|\alpha\beta\alpha\rangle] - 2E_q - E_{d'}\} \\
 &= \frac{1}{3}(6 \times 5.5 - 2 \times 4.1 - 5) = 6.6 \text{ eV}. \quad (D6)
 \end{aligned}$$

APPENDIX E: OPTICALLY DETECTED MAGNETIC RESONANCE SIGNAL

In this section, we study the effect of changing parameters used for ODMR signal in Table VI other than those discussed in the main text. In each of the following figures, we change only one or two parameters to see their effect on our model. Figure 9 shows that for different values of transition rates k_{57} and k_{68} we can see an ODMR signal. In Fig. 10, we checked the effect of changing the first- and second-excited state spin splittings ω_e and ω_{e2} . The result shows that, although changing them would affect the magnitude of the ODMR signal, there is only one resonance in the ODMR signal, which

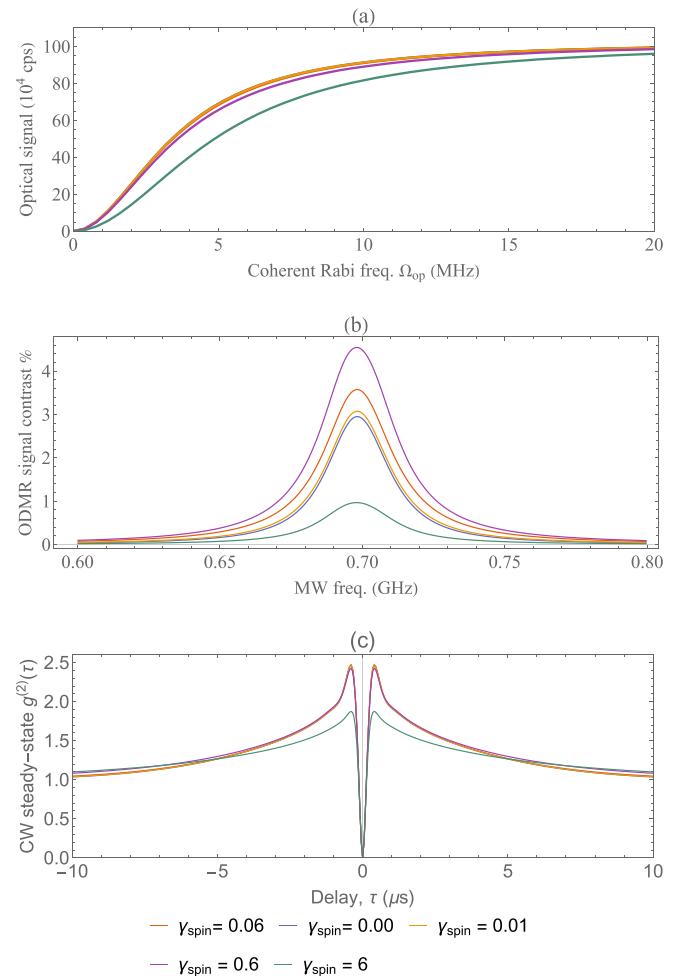


FIG. 11. The effect of changing γ_{spin} on the optical signal, ODMR contrast, and the second-order correlation function. All the variables are in MHz.

suggests that the signals are not narrow enough to distinguish the peaks of ω_e and ω_{e2} . Lastly, Fig. 11 shows that the spin relaxation times in the range of 0.06 MHz do not have a

significant impact on the ODMR signal. Only very large spin-relaxation times, which are very unlikely, decrease the ODMR signal.

-
- [1] D. D. Awschalom, L. C. Bassett, A. S. Dzurak, E. L. Hu, and J. R. Petta, Quantum spintronics: Engineering and manipulating atom-like spins in semiconductors, *Science* **339**, 1174 (2013).
- [2] J. R. Weber, W. F. Koehl, J. B. Varley, A. Janotti, B. B. Buckley, C. G. V. de Walle, and D. D. Awschalom, Quantum computing with defects, *Proc. Natl. Acad. Sci. USA* **107**, 8513 (2010).
- [3] I. Aharonovich, D. Englund, and M. Toth, Solid-state single-photon emitters, *Nat. Photonics* **10**, 631 (2016).
- [4] J. L. O'Brien, Optical quantum computing, *Science* **318**, 1567 (2007).
- [5] H. J. Kimble, The quantum internet, *Nature (London)* **453**, 1023 (2008).
- [6] M. Atatüre, D. Englund, N. Vamivakas, S.-Y. Lee, and J. Wrachtrup, Material platforms for spin-based photonic quantum technologies, *Nat. Rev. Mater.* **3**, 38 (2018).
- [7] T. T. Tran, K. Bray, M. J. Ford, M. Toth, and I. Aharonovich, Quantum emission from hexagonal boron nitride monolayers, *Nat. Nanotechnol.* **11**, 37 (2016).
- [8] F. Xia, H. Wang, D. Xiao, M. Dubey, and A. Ramasubramaniam, Two-dimensional material nanophotonics, *Nat. Photonics* **8**, 899 (2014).
- [9] G. Cassaboïs, P. Valvin, and B. Gil, Hexagonal boron nitride is an indirect bandgap semiconductor, *Nat. Photonics* **10**, 262 (2016).
- [10] C. Elias, P. Valvin, T. Pelini, A. Summerfield, C. J. Mellor, T. S. Cheng, L. Eaves, C. T. Foxon, P. H. Beton, S. V. Novikov, B. Gil, and G. Cassaboïs, Direct band-gap crossover in epitaxial monolayer boron nitride, *Nat. Commun.* **10**, 2639 (2019).
- [11] N. R. Jungwirth, B. Calderon, Y. Ji, M. G. Spencer, M. E. Flatté, and G. D. Fuchs, Temperature dependence of wavelength selectable zero-phonon emission from single defects in hexagonal boron nitride, *Nano Lett.* **16**, 6052 (2016).
- [12] A. L. Exarhos, D. A. Hopper, R. N. Patel, M. W. Doherty, and L. C. Bassett, Magnetic-field-dependent quantum emission in hexagonal boron nitride at room temperature, *Nat. Commun.* **10**, 222 (2019).
- [13] N. V. Proscia, Z. Shotan, H. Jayakumar, P. Reddy, C. Cohen, M. Dollar, A. Alkauskas, M. Doherty, C. A. Meriles, and V. M. Menon, Near-deterministic activation of room-temperature quantum emitters in hexagonal boron nitride, *Optica* **5**, 1128 (2018).
- [14] K. Konthasinghe, C. Chakraborty, N. Mathur, L. Qiu, A. Mukherjee, G. D. Fuchs, and A. N. Vamivakas, Rabi oscillations and resonance fluorescence from a single hexagonal boron nitride quantum emitter, *Optica* **6**, 542 (2019).
- [15] T. T. Tran, C. Elbadawi, D. Totonjian, C. J. Lobo, G. Grosso, H. Moon, D. R. Englund, M. J. Ford, I. Aharonovich, and M. Toth, Robust multicolor single photon emission from point defects in hexagonal boron nitride, *ACS Nano* **10**, 7331 (2016).
- [16] N. Mendelson, D. Chugh, J. R. Reimers, T. S. Cheng, A. Gottscholl, H. Long, C. J. Mellor, A. Zettl, V. Dyakonov, P. H. Beton, S. V. Novikov, C. Jagadish, H. H. Tan, M. J. Ford, M. Toth, C. Bradac, and I. Aharonovich, Identifying carbon as the source of visible single-photon emission from hexagonal boron nitride, *Nat. Mater.* **20**, 321 (2021).
- [17] M. Abdi, J.-P. Chou, A. Gali, and M. B. Plenio, Color centers in hexagonal boron nitride monolayers: A group theory and *ab initio* analysis, *ACS Photonics* **5**, 1967 (2018).
- [18] G. Grosso, H. Moon, B. Lienhard, S. Ali, D. K. Efetov, M. M. Furchi, P. Jarillo-Herrero, M. J. Ford, I. Aharonovich, and D. Englund, Tunable and high-purity room temperature single-photon emission from atomic defects in hexagonal boron nitride, *Nat. Commun.* **8**, 705 (2017).
- [19] H. L. Stern, Q. Gu, J. Jarman, S. E. Barker, N. Mendelson, D. Chugh, S. Schott, H. H. Tan, H. Sirringhaus, I. Aharonovich, and M. Atatüre, Room-temperature optically detected magnetic resonance of single defects in hexagonal boron nitride, *Nat. Commun.* **13**, 618 (2022).
- [20] A. Reserbat-Plantey, I. Epstein, I. Torre, A. T. Costa, P. A. D. Gonçalves, N. A. Mortensen, M. Polini, J. C. W. Song, N. M. R. Peres, and F. H. L. Koppens, Quantum nanophotonics in two-dimensional materials, *ACS Photonics* **8**, 85 (2021).
- [21] A. Dietrich, M. W. Doherty, I. Aharonovich, and A. Kubanek, Solid-state single photon source with Fourier transform limited lines at room temperature, *Phys. Rev. B* **101**, 081401(R) (2020).
- [22] C. Jara, T. Rauch, S. Botti, M. A. L. Marques, A. Norambuena, R. Coto, J. E. Castellanos-Águila, J. R. Maze, and F. Muñoz, First-principles identification of single photon emitters based on carbon clusters in hexagonal boron nitride, *J. Phys. Chem. A* **125**, 1325 (2021).
- [23] M. Hoesé, P. Reddy, A. Dietrich, M. K. Koch, K. G. Fehler, M. W. Doherty, and A. Kubanek, Mechanical decoupling of quantum emitters in hexagonal boron nitride from low-energy phonon modes, *Sci. Adv.* **6**, eaba6038 (2020).
- [24] P. Auburger and A. Gali, Towards *ab initio* identification of paramagnetic substitutional carbon defects in hexagonal boron nitride acting as quantum bits, *Phys. Rev. B* **104**, 075410 (2021).
- [25] C. Hepp, T. Müller, V. Waselowski, J. N. Becker, B. Pingault, H. Sternschulte, D. Steinmüller-Nethl, A. Gali, J. R. Maze, M. Atatüre, and C. Becher, Electronic Structure of the Silicon Vacancy Color Center in Diamond, *Phys. Rev. Lett.* **112**, 036405 (2014).
- [26] A. Sajid, J. R. Reimers, and M. J. Ford, Defect states in hexagonal boron nitride: Assignments of observed properties and prediction of properties relevant to quantum computation, *Phys. Rev. B* **97**, 064101 (2018).
- [27] M. W. Doherty, N. B. Manson, P. Delaney, and L. C. L. Hollenberg, The negatively charged nitrogen-vacancy centre in diamond: The electronic solution, *New J. Phys.* **13**, 025019 (2011).
- [28] J. R. Maze, A. Gali, E. Togan, Y. Chu, A. Trifonov, E. Kaxiras, and M. D. Lukin, Properties of nitrogen-vacancy centers in diamond: The group theoretic approach, *New J. Phys.* **13**, 025025 (2011).
- [29] M. W. Doherty, F. Dolde, H. Fedder, F. Jelezko, J. Wrachtrup, N. B. Manson, and L. C. L. Hollenberg, Theory of the ground-state spin of the NV⁻ center in diamond, *Phys. Rev. B* **85**, 205203 (2012).
- [30] D. Manzano, A short introduction to the Lindblad master equation, *AIP Adv.* **10**, 025106 (2020).

- [31] G. Noh, D. Choi, J.-H. Kim, D.-G. Im, Y.-H. Kim, H. Seo, and J. Lee, Stark tuning of single-photon emitters in hexagonal boron nitride, *Nano Lett.* **18**, 4710 (2018).
- [32] M. Tinkham, *Group Theory and Quantum Mechanics* (Courier Corporation, Mineola, New York, 2003).
- [33] K. Momma and F. Izumi, Vesta 3 for three-dimensional visualization of crystal, volumetric and morphology data, *J. Appl. Crystallogr.* **44**, 1272 (2011).
- [34] *Reviews in Computational Chemistry*, edited by K. B. Lipkowitz and D. B. Boyd (Wiley-VCH, New York, 2001), Vol. 17, Chap. 3.
- [35] M. L. Goldman, M. W. Doherty, A. Sipahigil, N. Y. Yao, S. D. Bennett, N. B. Manson, A. Kubanek, and M. D. Lukin, State-selective intersystem crossing in nitrogen-vacancy centers, *Phys. Rev. B* **91**, 165201 (2015).
- [36] M. L. Goldman, A. Sipahigil, M. W. Doherty, N. Y. Yao, S. D. Bennett, M. Markham, D. J. Twitchen, N. B. Manson, A. Kubanek, and M. D. Lukin, Phonon-Induced Population Dynamics and Intersystem Crossing in Nitrogen-Vacancy Centers, *Phys. Rev. Lett.* **114**, 145502 (2015).
- [37] C. Simon, M. Afzelius, J. Appel, A. B. de la Giroday, S. J. Dewhurst, N. Gisin, C. Y. Hu, F. Jelezko, S. Kröll, J. H. Müller, J. Nunn, E. S. Polzik, J. G. Rarity, H. D. Riedmatten, W. Rosenfeld, A. J. Shields, N. Sköld, R. M. Stevenson, R. Thew, I. A. Walmsley, et al., Quantum memories, *Eur. Phys. J. D* **58**, 1 (2010).
- [38] G. D. Fuchs, G. Burkard, P. V. Klimov, and D. D. Awschalom, A quantum memory intrinsic to single nitrogen–vacancy centres in diamond, *Nat. Phys.* **7**, 789 (2011).
- [39] J. H. Shim, I. Niemeyer, J. Zhang, and D. Suter, Room-temperature high-speed nuclear-spin quantum memory in diamond, *Phys. Rev. A* **87**, 012301 (2013).
- [40] M. Auzinsh, A. Berzins, D. Budker, L. Busaite, R. Ferber, F. Gahbauer, R. Lazda, A. Wickenbrock, and H. Zheng, Hyperfine level structure in nitrogen-vacancy centers near the ground-state level anticrossing, *Phys. Rev. B* **100**, 075204 (2019).
- [41] A. M. Stoneham, *Theory of Defects in Solids: Electronic Structure of Defects in Insulators and Semiconductors* (Clarendon Press; Oxford University Press, New York, 2001).
- [42] M. Mackoit-Sinkevičienė, M. Maciaszek, C. G. V. de Walle, and A. Alkauskas, Carbon dimer defect as a source of the 4.1 eV luminescence in hexagonal boron nitride, *Appl. Phys. Lett.* **115**, 212101 (2019).
- [43] Á. Gali, Ab initio theory of the nitrogen-vacancy center in diamond, *Nanophotonics* **8**, 1907 (2019).
- [44] S.-Y. Lee, T.-Y. Jeong, S. Jung, and K.-J. Yee, Refractive index dispersion of hexagonal boron nitride in the visible and near-infrared, *Phys. Status Solidi B* **256**, 1800417 (2019).
- [45] A. Alkauskas, Q. Yan, and C. G. Van de Walle, First-principles theory of nonradiative carrier capture via multiphonon emission, *Phys. Rev. B* **90**, 075202 (2014).
- [46] F. Wu, T. J. Smart, J. Xu, and Y. Ping, Carrier recombination mechanism at defects in wide band gap two-dimensional materials from first principles, *Phys. Rev. B* **100**, 081407(R) (2019).
- [47] M. E. Turiansky, A. Alkauskas, M. Engel, G. Kresse, D. Wickramaratne, J.-X. Shen, C. E. Dreyer, and C. G. Van de Walle, Nonrad: Computing nonradiative capture coefficients from first principles, *Comput. Phys. Commun.* **267**, 108056 (2021).
- [48] A. Gottscholl, M. Kianinia, V. Soltamov, S. Orlinskii, G. Mamin, C. Bradac, C. Kasper, K. Krambrock, A. Sperlich, M. Toth, I. Aharonovich, and V. Dyakonov, Initialization and read-out of intrinsic spin defects in a van der Waals crystal at room temperature, *Nat. Mater.* **19**, 540 (2020).
- [49] N. Chejanovsky, A. Mukherjee, J. Geng, Y.-C. Chen, Y. Kim, A. Denisenko, A. Finkler, T. Taniguchi, K. Watanabe, D. B. R. Dasari, P. Auburger, A. Gali, J. H. Smet, and J. Wrachtrup, Single-spin resonance in a van der Waals embedded paramagnetic defect, *Nat. Mater.* **20**, 1079 (2021).
- [50] T. Nakamura, M. Wada, K. Okada, A. Takamine, Y. Ishida, Y. Yamazaki, T. Kambara, Y. Kanai, T. M. Kojima, Y. Nakai, N. Oshima, A. Yoshida, T. Kubo, S. Ohtani, K. Noda, I. Katayama, V. Lioubimov, H. Wollnik, V. Varentsov, and H. A. Schuessler, Laser spectroscopy of $^{7,10}\text{Be}^+$ in an online ion trap, *Phys. Rev. A* **74**, 052503 (2006).
- [51] D. H. Slichter, V. B. Verma, D. Leibfried, R. P. Mirin, S. W. Nam, and D. J. Wineland, UV-sensitive superconducting nanowire single photon detectors for integration in an ion trap, *Opt. Express* **25**, 8705 (2017).
- [52] G. Clos, M. Enderlein, U. Warring, T. Schaetz, and D. Leibfried, Decoherence-Assisted Spectroscopy of a Aingle Mg^+ Ion, *Phys. Rev. Lett.* **112**, 113003 (2014).
- [53] M. K. Boll, I. P. Radko, A. Huck, and U. L. Andersen, Photophysics of quantum emitters in hexagonal boron-nitride nano-flakes, *Opt. Express* **28**, 7475 (2020).
- [54] A. Gottscholl, M. Diez, V. Soltamov, C. Kasper, A. Sperlich, M. Kianinia, C. Bradac, I. Aharonovich, and V. Dyakonov, Room temperature coherent control of spin defects in hexagonal boron nitride, *Sci. Adv.* **7**, eabf3630 (2021).
- [55] P. Giannozzi, S. Baroni, N. Bonini, M. Calandra, R. Car, C. Cavazzoni, D. Ceresoli, G. L. Chiarotti, M. Cococcioni, I. Dabo, et al., Quantum espresso: A modular and open-source software project for quantum simulations of materials, *J. Phys.: Condens. Matter* **21**, 395502 (2009).
- [56] P. E. Blöchl, Projector augmented-wave method, *Phys. Rev. B* **50**, 17953 (1994).
- [57] J. P. Perdew, K. Burke, and M. Ernzerhof, Generalized Gradient Approximation Made Simple, *Phys. Rev. Lett.* **77**, 3865 (1996).
- [58] F. Ferreira, A. Chaves, N. Peres, and R. Ribeiro, Excitons in hexagonal boron nitride single-layer: A new platform for polaritonics in the ultraviolet, *J. Opt. Soc. Am. B* **36**, 674 (2019).
- [59] J. Heyd, G. E. Scuseria, and M. Ernzerhof, Hybrid functionals based on a screened Coulomb potential, *J. Chem. Phys.* **118**, 8207 (2003).
- [60] D. Wickramaratne, L. Weston, and C. G. V. de Walle, Monolayer to bulk properties of hexagonal boron nitride, *J. Phys. Chem. C* **122**, 25524 (2018).
- [61] A. Gali, E. Janzén, P. Deák, G. Kresse, and E. Kaxiras, Theory of Spin-Conserving Excitation of the N-V^- Center in Diamond, *Phys. Rev. Lett.* **103**, 186404 (2009).
- [62] J. R. Reimers, A. Sajid, R. Kobayashi, and M. J. Ford, Understanding and calibrating density-functional-theory calculations describing the energy and spectroscopy of defect sites in hexagonal boron nitride, *J. Chem. Theory Comput.* **14**, 1602 (2018).
- [63] D. H. Ess, E. R. Johnson, X. Hu, and W. Yang, Singlet-triplet energy gaps for diradicals from fractional-spin density-functional theory, *J. Phys. Chem. A* **115**, 76 (2011).
- [64] K. Li, T. Smart, and Y. Ping, C_2CN as a 2 eV single-photon emitter candidate in hexagonal boron nitride, [arXiv:2110.01787](https://arxiv.org/abs/2110.01787).